Climatic influence of the latest Antarctic isotope maximum of the last glacial period (AIM4) on Southern Patagonia

Guillaume Jouve [a,b,c*], Agathe Lisé-Pronovost [d], Pierre Francus [a,b], Arnaud S. De Coninck [a,b] and the PASADO Science Team [e]

[a]Centre Eau, Terre et Environnement, Institut National de la Recherche Scientifique, Québec, Canada.

[b]GEOTOP Research Center, Montréal, Canada.

[c]Centre Européen de Recherche et d'enseignement des Géosciences de l'Environnement (CEREGE), Aix-Marseille University, Aix-en-Provence, France.[1]

[d]The Australian Archeomagnetism Laboratory, La Trobe University, Melbourne, Australia.

[e]PASADO science team as listed at http://www.icdp-online.org/front_content.php?idcat=1494

[*]corresponding author

Guillaume Jouve : (418) 654 2530-4480 jouve@cerege.fr

Agathe Lisé-Pronovost : +61 03 9479 1392 a.lise-pronovost@latrobe.edu.au

Pierre Francus : (418) 654 3780 pierre.francus@ete.inrs.ca

Arnaud de Coninck : (418) 654 3704 arnaud.de_coninck@ete.inrs.ca

[1] Present address of the corresponding author

Abstract

This paper presents the first detailed paleoclimate reconstruction of the latest Antarctic isotope maximum (AIM4, ~33-29 ka cal. BP) at 52°S in continental southeastern Argentine Patagonia. High-resolution sedimentological and geochemical analyses of sediments from the maar lake Potrok Aike (PTA) reveal a decrease in the thickness of flood-induced turbidites and a series of wind burst deposits during AIM4, both pointing to increasingly drier conditions. This interpretation is also supported by a significant amount of runoff-driven micropumices incorporated within the sediments that suggests a lower lake level with canyons incising thick tephra deposits around the lake. Increased gustiness and/or dust availability in southeast Patagonia, together with intensified Antarctic circumpolar circulation in the Drake Passage, dust deposition in the Scotia Sea and in Antarctica ice shelf, are consistent with a southward shift of the Southern Westerly Winds (SWW) during the AIM4. In contrast to other warmer AIMs, the SWW during the AIM4 did not migrate far enough south to generate upwelling in the Southern Ocean and they did not reach 52°S in SE Patagonia, as revealed by unchanged values of the rock-magnetic proxy of wind intensity obtained from the same PTA core. Nevertheless, the SWW displacement during AIM4 imposed drier conditions at 52°S in southeast Patagonia likely by blocking precipitation from the Atlantic Ocean, in a way similar to modern seasonal variations and the other Antarctic warm events.

Keywords**:** Southern Westerly Winds, micro X-ray fluorescence, microfacies, micropumices, dust, flood.

1. Introduction

The Southern Westerly Winds (SWW) dominate the atmospheric circulation of the Southern Hemisphere subpolar and mid latitudes, and modify upwelling of carbon-rich deep water around Antarctica (Kuhlbrodt et al., 2007; Sijp and England, 2009; Toggweiler and Samuels, 1995) and in the Southern Ocean (Anderson et al., 2009; d'Orgeville et al., 2010; Menviel et al., 2008; Toggweiler et al., 2006; Tschumi et al., 2008). Moreover, any change in the SWW position and strength affects the precipitation pattern on land, over southern Australia (Petherick et al, 2013) and southern South America (Mayr et al., 2007b; Pollock and Bush, 2013; Schneider et al., 2003). In Patagonia, lakes between 51 and 55°S are situated at the interface between the southern limit of the SWW belt during the Last Glacial (Kaiser et al., 2005; Lamy et al., 2004; Ledru et al., 2005), located further north, and the current southern limit of the SWW belt (Hodgson and Sime, 2010; Lamy et al., 2010; Mcglone et al., 2010). The extraction of paleohydrological and paleowind information from the sedimentary record of those lakes can thus reveal SWW latitudinal shifts over time. Reaching back 51 ka cal. BP, the 106.9 meter-long sedimentary composite sequence from the International Continental scientific Drilling Program - Potrok Aike Maar Lake Sediment Archive Drilling project (ICDP-PASADO) (Fig. 1) is the only continuous continental archive going back to the last glacial period in southern South America and represents a unique opportunity to reconstruct paleohydrological and paleowind changes to be compared with the Antarctic ice cores records (Hahn et al., 2014, 2013; Jouve et al., 2013; Kliem et al., 2013b; Lisé-Pronovost et al., 2015, 2014; Recasens et al., 2015, 2011; Schäbitz et al., 2013; Zhu et al., 2013; Zolitschka et al., 2013).

Marine Isotope Stage 3 (MIS3) is a climatic period of the Last Glacial, spanning from 60 to 29 thousand years ago in calibrated ages (cal. BP), marked by several maxima in the $\delta^{18}O$ of gas trapped in Antarctica's ice (Antarctic Isotope Maxima, AIM). These are reflecting increases in Antarctic temperatures called Antarctic warm events (Blunier and Brook, 2001; Blunier et al., 1997). The most recent Antarctic warm event AIM4 (from 33 to 29 ka cal. BP), was characterized by a slight increase in Antarctica temperatures and a drastic fourfold increase of dust deposited in eastern Antarctica (Barbante et al., 2006) (dust mass from ca. 200 to 800 p.p.b.; Fig. 2b). Magnetic susceptibility of sediments from the Scotia Sea also indicate important input of dust during AIM4 (Weber et al., 2012) (Fig. 2). The source of dust for these regions during glacial times was southern Patagonia (Basile et al., 1997; Delmonte et al., 2010, 2004; Petit et al., 1999; Sugden et al., 2009).

Sugden et al. (2009) did not find glacial landscape evidence in Patagonia to account for the increased Patagonian dust loading of the atmosphere during AIM4. Nevertheless they noted that around 30 ka there were multiple glacier advances in the Strait of Magellan. Could a dustier southern hemisphere atmosphere be linked to barren land without vegetation just before glacier growth and when they retreated from their outwash plains? How did climate change in southern Patagonia during AIM4?

At the core of the dust source region, Laguna Potrok Aike (PTA) records a sharp increase in low field magnetic susceptibility (k_{LF}) values during AIM4 (Lisé-Pronovost et al., 2015). High k_{LF} values were maintained until the deglaciation around 17.3 ka, when they sharply decreased as more organic sediments diluted the proportion of ferrimagnetic minerals. Detailed rock-magnetic analysis revealed that these higher k_{LF} values reflect greater amount of detrital ferrimagnetic grains reaching the lake (Lisé-Pronovost et al., 2015, 2014, 2013). No other paleoenvironmental indicator measured from PTA displays such sharp and large amplitude change over the entire 51.2 ka record (Zolitschka et al., 2013). Yet the cause of this sharp k_{LF} change during AIM4 remains unknown. What is known is that the wind intensities at PTA during Marine Isotope Stage 3 were relatively weaker than the Holocene (Lisé-

Pronovost et al., 2015), as also indicated by several proxy records from which a northward shift of the SWW belt by about 5–6° latitude during glacial periods has been inferred (Kaiser et al., 2005; Kohfeld et al., 2013; Lamy et al., 2004; Ledru et al., 2005; Pollock and Bush, 2013). Therefore, there is a discrepancy between the wind intensity and the amount of ferrimagnetic grains transported to the lake between 33 and 17.3 ka cal. BP.

This paper presents some evidence addressing these issues using the first detailed and continuous record of AIM4 in continental Patagonia. Specifically, it aims to test several hypotheses that can explain the shift that occurred during the AIM4 interval at PTA, and to improve the understanding of changes in dustiness and climate at the hemispheric scale during this interval. The paper presents elemental composition (micro-X-ray fluorescence: µ-XRF), grain size and Principal Component Analyses (PCA) of µ-XRF data of PTA sediments along the entire AIM4 interval, to disentangle the hydrological from the aeolian signal of the PTA lacustrine deposits.

2. Study site

PTA is situated in the Pali Aike Volcanic Field (PAVF) in Argentine Patagonia, located about 70 km north of the Strait of Magellan, 100 km west of the Atlantic coast and 1,500 km north of Antarctica (Fig. 1). Situated in the back arc Patagonian plateau lavas, the PAVF has a maximum W-E extension of about 150 km, and a maximum N-S extension of approximately 50 km and covers an area of about 4500 km^2 (Skewes, 1978; D’Orazio et al., 2000; Mazzarini and D’Orazio, 2003). PTA is a maar lake, resulting from a phreatomagmatic eruption, dated around 0.77 +/- 0.24 Ma by Ar/Ar (Zolitschka et al., 2006). Maar volcanoes, plateau lavas and scoria cones prevail in the catchment area. PTA is a nearly circular lake, has a maximum diameter of 3,470 meters, and a maximum water depth of about 100 meters (Haberzettl et al., 2005; Zolitschka et al., 2009). Its watershed has an area close to 200 km^2 (Haberzettl et al., 2005). The prevailing SWW (average 9 $m.s^{-1}$ at the beginning of the summer; Endlicher, 1993) and the Andes Mountains cause a strong climatic contrast within Patagonia. Indeed, due to the rain shadow effect of the Andes Mountains, most of southeastern South America is semiarid steppes, with annual precipitation below 300 $mm.a^{-1}$ (González and Rial, 2004; Haberzettl et al., 2009; Mayr et al., 2007a; McCulloch et al., 2000). The PTA watershed is covered by a dry type of Magellanic steppe vegetation is mainly represented by *Festuca gracillima* (Wille et al., 2007). Stands of *Acaena* sp., *Adesmia boronioides* (high shrubs), some grasses (*Festuca*, *Poa* and *Stipa* sp.) mixed with other plants like *Colobanthus subulatus* occur around the lake (Wille et al., 2007). In southeastern South America, the weaker the SWW, the more important is precipitation coming from the Atlantic (Mayr et al., 2007b; Schneider et al., 2003). Because neither inflow nor outflow currently exists at PTA, the lake level is mainly controlled by the evaporation/precipitation ratio. Thus, high lake level occurs during wet years and vice versa (Haberzettl et al., 2005; Kliem et al., 2013b; Ohlendorf et al., 2013). This relationship between the hydrology of Lake Potrok Aike and the SWW through time is recorded by the pelagic sediments of Lake Potrok Aike (Zolitschka et al., 2013 and references therein). Consequently, the geographical, climatic and geomorphological setting of PTA suggest that detrital sediments are brought to the lake primarily by wind and episodically by precipitation runoff (Lisé-Pronovost et al., 2014).

3. Material and methods

3.1 Field work

In the framework of the ICDP, drilling was conducted with the GLAD800 drilling system using a hydraulic piston core. From August to November 2008, two primary sites were drilled at a depth of about 100 meters: 5022-1 (PTA 1) and 5022-2 (PTA 2) (Kliem et al., 2013a; Ohlendorf et al., 2011) (Fig. 1). The entire 106.9 meter-long composite sedimentary sequence was constructed from the combination of cores retrieved from three holes (A, B and C) at site 5022-2 (Fig. 1). Correlations were done considering stratigraphic markers (lithological facies and tephras) and magnetic susceptibility (Kliem et al., 2013a). This profile is the local reference sedimentary sequence used by scientists involved in the PASADO project (Ohlendorf et al., 2011).

3.2 Stratigraphy and chronology

Pelagic sediments (about 45% of the entire PASADO sequence) are represented by continuous settling of particles under mean climate state conditions and consist of laminated silts and sands (Haberzettl et al., 2007; Jouve et al., 2013; Kliem et al., 2013a). Mass movement deposits (about 55%, reworked sediments), including tephras and reworked tephra layers (about 4.5%), were diagnosed using macroscopic and stratigraphic observations (Kliem et al., 2013a; Wastegård et al., 2013). The entire sedimentary sequence was divided into lithostratigraphic units A, B, C-1, C-2, C-3 (Kliem et al., 2013a) (Fig. 2a). The studied sedimentary interval, i.e. 40.62 to 37.90 meters composite depth (m cd), falls within two lithostratigraphic units: C-1 and C-2 (Fig. 2a). Both units are mostly composed of pelagic laminated silts intercalated with thin fine sand and coarse silt layers (Kliem et al., 2013a). The main difference between these two units is the percentage of mass movement deposits that is lower in C-1. The boundary between these units is at 40.23 m cd.

This paper uses the radiocarbon-based age model established by Kliem et al. (2013a) (Fig. 2). The chronology was built from 58 radiocarbon dates following a mixed-effect regression procedure (Fig. 2a) and the chronology is supported by magnetostratigraphy in the older part of the record (Kliem et al., 2013a). One radiocarbon date (i.e., 40.09 m cd; Fig. 3) in the lower part of the analysed sequence constrains the chronology at 33.7 ka cal. BP +/- 0.4 (Kliem et al., 2013a) and was performed on stems of aquatic mosses. According to the age model (Fig.2), the 40.62 to 37.90 meters composite depth (m cd) interval spans from 33.7 to 30.6 ka cal. BP (yellow-shaded interval in Fig. 2b). It corresponds to the beginning of a drastic increase in the magnetic susceptibility in Scotia sea sediments, as well as in the dust mass in EPICA Dome C ice cores (Fig. 2b). According to the PASADO age model (Kliem et al., 2013a), the Mount Burney (52°S in the Austral Andean volcanic zone) tephra layer between 38.73 and 38.7 m cd (Fig. 3), was deposited 31.2 +/- 1.3 ka cal. BP (Wastegård et al., 2013).

3.3 Thin section and image analysis

An interval of 2.72 meters of sediments was subsampled perpendicular to bedding with aluminium slabs using a “cheese-cutter style” tool (Francus and Asikainen, 2001) from 40.62 to 37.90 m cd. Slabs were then freeze dried and impregnated with Spurr’s low velocity epoxy resin (Lamoureux, 1994), before being prepared as thin-sections. Tagged Image File Format (Tiff) images were retrieved in high-resolution (2,400 dots per inch, dpi) using a flatbed transparency scanner under natural and cross-polarized light (De Keyser, 1999; Lamoureux and Bollmann, 2004). The images were then imported and observed by an image analysis software developed at INRS-ETE (Francus and Nobert, 2007; Francus, 1998). The software allows the detection of regions of interest (ROI) within thin-sections and, driving a scanning electron microscope (Model: Carl Zeiss EVO® 50 smart SEM), the automatic acquisition of backscattered electron (BSE) images of those ROIs. An accelerating voltage of 20 kV and a working distance of 8.5 mm were used to achieve these images. Then, the original grey-scale BSE image is transformed into a black and white image revealing the sedimentary particles in their matrix (Francus, 1998). Only particles larger than 3 µm can be accurately measured, leaving the clay particle out of the measurements. Afterwards, measurements of area, center of gravity, length of major axis, and minor axis of the best fitting ellipse can be made on each particle. These measurements are saved in a spreadsheet for further processing (Francus and Karabanov, 2000). Details of the algorithms used in this study are available in supplementary materials of Jouve et al. (2013). The software weights each particle by assuming they are spherical quartz grains (Francus et al., 2002) by using the following formula: $((4/3)*\pi*((D_0/2)^3))*2.65$, with D_0 being the equivalent disk diameter. Even if the random two-dimensional section does not systematically cut grains through their center of gravity, which under-estimate the grain diameter (Bui and Mermut, 1989; Russ, 1992; Bouabid et al., 1992), image analysis grain size has proven to be well correlated with petrographic microscope grain size measurements (Francus et al., 2002). Particle weight is then summed for each particle size class and class percentages can be calculated. At the end, the sediment is classified according to Krumbein and Sloss (1963).

3.4 Micro X-ray fluorescence

Non-destructive microgeochemical analyses (µ-XRF) were performed on U-channels with an ITRAX core scanner (INRS-ETE, Québec). The instrument (Cox Analytical systems, Mölndal, Sweden) (Croudace et al., 2006) used a 3 kW molybdenum target tube set to 30kV and 25mA. Acquisition of continuous µ-XRF has been performed at a 0.1 mm scale with an exposure time of 15s. The numbers of counts for each element in each spectrum acquired for a specific depth interval was normalized by the total number of counts of that spectrum (expressed in kcps, i.e. 1000 counts per second).

3.5 Principal Component Analysis (PCA)

As both µ-XRF and rock-magnetic analyses were conducted on the same u-channels, there is no lag between these data. µ-XRF data were averaged every cm to fit with the 1-cm resolution rock-magnetic measurements. PCA was conducted on µ-XRF data using the significant elements present in the PASADO sedimentary sequence, i.e. Si, Ca, Ti, Fe, Mn, K, Ni, V, Sr, Zr and Rb (Hahn et al., 2014). Elemental data were previously centered to zero by subtraction of averages and scaled with its variance in order to give each element equal importance. Details on PCA analyses are available in Table 1, while descriptive statistics of the analyses are in Appendix D.

3.6 Laser diffraction grain size analyses

Two hundreds and six samples were analyzed using a LS 200 laser particle size analyzer from Beckman Coulter, USA equipped with a fluid module. The sampling resolution was every 0.5 cm to every 10 cm depending on the sediment macroscopic facies. The greater the homogeneity of the sediment facies, the lower was the sampling resolution. The analyses were performed at Queen's University (Canada). The samples passed completely through a 1-mm sieve and were treated three successive times with 30% H_2O_2 to remove organics followed by 1 M NaOH to remove biogenic silica (Last and Smol, 2002). Samples were then manually introduced into the analyzer and underwent three successive 60-seconds runs using continuous sonication to disperse aggregated particles (McDonald and Lamoureux, 2009). All statistical grain-size parameters were calculated with the Gradistat software (Blott and Pye, 2001) using the Folk and Ward graphical method (Folk and Ward, 1957). Two sigma (SD) error bars (5% of the values) are shown, representing the reproducibility of data from laser diffraction analyses of fine-grained sediment (<10µm) (Sperazza et al., 2004). The uncertainty increases with the clay content. Consequently, these error bars are plotted, to show the maximum error possible for our, mainly, silty clay or silty sand sediments.

4. Results

The sequence investigated here is composed of greenish-grey, unconsolidated, partly laminated clastic sediments with several graded beds, sand layers, and two tephras (Fig. 3a). This continuous interval is described for the following: facies and microfacies architecture (microfabrics), grain size and statistical analyses of the elemental geochemistry. The three first significant principal components represent about 53% of the total variability. Details on (1) macroscopic observation (cm-scale) of facies with XRF and laser diffraction grain size signature are available in Figure 4, (2) microsedimentary structures with BSE and image analysis grain size of microfacies in Figures 5, (3) additional information on facies in Figure 6 and Appendix B, (4) µ-XRF data in Appendix A.

4.1 Facies assemblage 1

Laser diffraction grain size analysis reveals four normally graded beds (facies 1) with a clay cap (facies 2) (Fig. 3, 5). Although their thicknesses are different, all four events are characterized by grain-supported medium to fine sand layers at the bottom facies 1 with an erosive basal contact (Fig. 5). They all include macrophyte remains and micropumices (i.e. microscopic fragment of pumices derived from tephra deposits; Fig. 5 and 6). The grain size of the coarser bottom part (facies 1) is represented by 80 to 95% sand (laser diffraction analysis). Image analysis grain size shows sub-rounded to rounded clastic sediments composed of about 85% sand and 15% silt (Fig. 5). Especially for event a and b, these layers correspond to peaks of PC2 (Fig. 3c and 4; Table 1; Appendix A), pointing out an elemental composition dominated by silicon- (Si, r_{PC2}=0.55), calcium (Ca, r_{PC2}=0.47), and strontium (Sr, r_{PC2}=0.42) (Table 1). Figure 4 allows the observation of the link between textural and geochemical signature of this facies assemblage at an appropriate scale.

Clayey silts overlie the sand (Fig. 6c). These finer sediments show peaks in PC1 (Fig. 3c), i.e. silt- and clay-rich sediments are rich in iron (Fe, r_{PC1}=0.81), titanium (Ti, r_{PC1}=0.7), and potassium (K, r_{PC1}=0.47) (Fig. 3b and c; Table 1).

4.2 Facies 3: sand layers

Images of sediment cores and laser diffraction grain size analyses reveal the presence of seven sand layers (yellow areas in Fig. 3a). Unlike facies 1, these layers are devoid of macrophyte remains, and do not have any erosive contact with the underlying sediments (Fig. 5). Sand layers 2 and 3 are however not observable in the sand result (Figure 3) because they fall between the sand layers. Laser diffraction analysis indicates facies 3 has 20 to 40% sands, in contrast to about 5% for background sediment. Microfacies analyses of these deposits reveals matrix-supported angular to rounded silty sands (Fig. 5). Image analysis of clastic grains attest of about 65% of sands and 35% of silts (Fig. 5). When compared (using image analysis) to the background, i.e. pelagic sediments, the sand concentration increases from 9 to 13 times (Fig. 7). The gradual decrease in sand, Ca and PC2 suggest a gentle fining upward deposit (Fig. 4). This figure also highlights the link between the textural and geochemical data at the appropriate scale.

4.3 Facies 4: pelagic deposit

This facies is homogenous, unlaminated and without any specific sedimentary structure (Fig. 4). These sediments are composed of matrix-supported angular to rounded silty clays to silty sands (Fig. 5). Image analysis of clastic grains attest to about 72% silt and 28% sand (Fig. 5). Micropumices are seldom present in this facies. The grain size is mainly represented by clayey (about 30%) silts (about 65%), with about 5% of sand particles (laser diffraction analysis).

4.4 Facies 5: Mt Burney tephra layer

This MIS3 Mt Burney tephra layer has already been discovered and described by Wastegård et al. (2013). It is present in the upper part of the sedimentary section under study (38.72 – 38.68 m cd; Fig. 3). This deposit has a specific geochemical signature as shown by a drastic decrease in Ti, Fe and K and increase in the Ca, Si and Sr (Fig. 4; Appendix A). At microscopic scale, this grain-supported facies displays a sharp contact with the underlying sediment (Fig. 5). The absence of any erosive structure, together with a clear dominance of volcanic minerals and micropumices (Fig. 5), show the regular and rapid deposit of pyroclastic ashes, fallen at the lake water surface after the eruptive event. The laser diffraction grain size of the tephra shows mainly sand at the bottom (about 60%) corresponding to the first volcanic minerals and the coarser fragments of pumice that fall in the lake after the eruption (Fig. 4). This is rapidly followed by silt (about 60%) that mainly corresponds to micropumice (Fig. 5).

4.5 Facies assemblage 2: reworked tephra layer

Another tephra layer is deposited between 38.04 – 38.02 m cd (Fig. 3, 5). This tephra has a microstructure drastically different from the Mt Burney tephra, facies 5 (Fig 5). Indeed, it shows a glass-shard matrix-supported sediment, with heterogenous and heterometric clastic grains, deposited with a discontinuous laminations (facies 7) and erosive structures (facies 6) with the underlying sediment. Previous macroscopic observation suggested this layer was a reworked tephra (Wastegård et al., 2013). The laser diffraction grain size of the reworked tephra is mainly represented by clayey (about 20%) silt (about 65%) (facies 7), with more sand in facies 6 (about 20%) (Fig. 3, 5).

4.6 Facies 8: micropumice-rich sediments

After the deposition of the Mt Burney tephra, a general decrease in clays and sands occurs. This is the only interval where clays and silts do not covary. Indeed, statistical analyses demonstrate that clays and silts are well correlated (R^2=0.7; Appendix C) below the Mt Burney tephra, while they are anti-correlated above it (R^2= 0.3; Appendix C). Silts steadily increase along this interval, as well as for PC3. PC3 is mainly controlled by the variability of Zr (r_{PC3} = 0.68; Table 1). Grain-size obtained by image analysis attests that clastic grains are 100% silts (Fig. 5). Under laser diffraction analysis, the grain size of this facies is about 70% silt (Fig. 3). Microfacies analysis reveal the presence of numerous silt-sized micropumices (Fig. 5).

5. Discussion

5.1Facies assemblage 1: Flood-induced turbidite

Graded beds are common features in lake sediments, where they are usually associated with turbidity currents triggered by either flood events or mass movements (Arnaud et al., 2002; Gilbert et al., 2006; Matter and Tucker, 1978; Mulder and Chapron, 2011; Shiki et al., 2000; Wilhelm et al., 2013). Following the work of Giguet-Covex et al. (2012) and (Wilhelm et al., 2013, 2011), normally graded beds detected in this study (Fig. 5; 6c) display the typical sedimentary structures of flood-induced turbidites. Indeed, grain-supported silty sands at their base are interpreted as hyperpycnite from flood-induced turbidity currents (Fig. 5; Fig. 3b; Arnaud et al., 2002; Mulder et al, 2003). The strength of the flow eroded the underlying sediment is demonstrated by erosive structures (Fig. 5). The integration of macrophyte remains supports this interpretation since they are currently abundant on the shoreline (Fig. 8) and can thus easily be incorporated by flood events. The overlying clayey silts sediments reflect the deposition of the finer fraction when the current velocity decreases. The thickness of these graded beds decrease up the sequence which, according to the model developed by Giguet-Covex et al. (2012) and Wilhelm et al. (2015, 2013), points to a decrease in the duration and/or intensity of the floods (Fig. 6).

5.2Facies 3: Dust storm event

As the Patagonian climatological pattern is mainly controlled by wind, the stronger the wind, the more the sediment integrates sands. Figure 8 shows photographs taken on the western part of the lake highlighting the amount of clastic particles that can be uplifted and transported to the lake during a wind gust. Gently fining upward matrix-supported silty sand layers deposited without any erosive structures, and devoid of macrophyte remains, are thus interpreted as the result of dust storm events (Fig. 5; Appendix B). Disentangling extreme versus less extreme dust storm events from such deposits requires deeper sedimentological analyses and remains speculative. Following the sedimentary depositional pattern of dust storm events described in this study, it seems however legitimate to consider that the greater the amount of the coarsest particles is important at the bottom of these facies (limits of the counting remain to be determined) the more they have required strong wind gusts to be uplifted. In this case, events 3, 5 and 7 could have been the strongest dust storm events recorded in this sequence. Similar episodic wind-driven “saltation burst” events are documented today in cold and dry desert such as Taylor Valley in Antarctica (Šabacká et al., 2012). From ~39.4 to ~38.8 m cd, seven dust storm events occurred during which Ca-, Si- and Sr-rich minerals were primarily transported by wind (Fig. 3; Appendix A). As several peaks in sands are present in the micropumice-rich interval, more dust events are suspected to be recorded (Fig. 5) but with different geochemical and structural fingerprints, which are difficult to identify because of the strong presence of micropumices.

5.3 Link between geochemistry and grain size of clastic sediments.

Hahn et al. (2014) conducted principal component analyses (PCA) on µ-XRF measurements for the entire PASADO records, and showed that sediments from the Glacial period are mainly characterized by Fe, Ti, K and Si, elements indicative of fine clastic grains, and by Ca and Sr, elements related to coarse-grained layers. This coarse-grained material is suggested to originate from a basalt outcrop at the western shore (Hahn et al., 2014; Kastner et al., 2010) that is rich in anorthite. In this study, sediments rich in clays and silts are also characterized by peaks in Fe, Ti and K (PC1). Sandy-rich sediments covary with the Ca, Si and Sr (PC2) that are represented by strong precipitation runoff or dust storm events. As the geochemical signature of sand layers and graded beds are quite similar (Fig. 4), the discrimination between dust storm events or flood-induced turbidites can only be performed using critera such as the presence of macrophyte, and erosive contact identifiable only in thin sections.

The other principal components are not relevant to this study since each of them represent less than 10% of the variability (Appendix D). Moreover, they are represented by trace elements (Ni, V, Mn and Rb) that have already been explained by Hahn et al. (2014) as linked to enforced oxic conditions at the water/sediment interface due to the wind intensity, whether during glacial or interglacial periods.

Peak shapes are different and not perfectly defined for each flood-induced turbidites (Fig. 3). This is probably due to the fact that the grain size of sediments is highly variable and causing substantial changes in the surface roughness, organic matter, water content and porosity which is proven to influence the accuracy of XRF scanning results (Croudace et al., 2006;

Löwenmark et al., 2011; Rothwell and Rack, 2006; St-Onge et al., 2007; Tjallingi et al., 2007; Weltje and Tjallingi, 2008). In consequence, the detection of elements can be slightly distorted, explaining some inaccuracies in the PCA analysis.

5.4 Facies assemblage and facies made of volcanic particles

5.4.1 Facies 8: micropumice-rich sediments

Immediately after the deposition of the Mt Burney tephra layer, silts and clays abundances are no longer correlated (Appendix C). Indeed, it changes from a strong correlation (R^2=0.7), to an anti-correlation of R^2=0.3, suggesting a change in particle source. Even if the anti-correlation could be driven by two distinct statistical populations, it remains that the relation between silt and clay no longer exists above the tephra layer. This change in the grain size behaviour is explained by the large amount of silt-sized micropumice (Fig. 5) present in this interval. The coarser the pumice fragments (sand peak) the more they can integrate clays in their vesicular structures. This may explain why sand and clay particles are covarying in these sediments. Hence, the geochemistry of the sediment is no longer primarily controlled by PC1 or PC2 but by PC3 (Fig. 3c), which is mainly driven by the relative concentration of Zr (r_{PC3} = 0.68; Fig. 3c; Table 1). This element is suggested to be a proxy of past atmospheric transport of materials derived from Hudson volcano tephras throughout the Patagonian region, the Scotia Sea and the Antarctica (Gaiero, 2007). Sapkota et al. (2007), and more recently Vanneste et al. (2015), also use the high content of Zr in acid insoluble ash from the Mt Burney volcano as a proxy of past atmospheric dust on peat bog cores in Tierra del Fuego (southern Chile). A tephra layer contains acid soluble and insoluble ashes. Waters running off an exposed tephra, after a lake level drop (see photograph in Fig. 8), can bring more acid insoluble than acid soluble ashes to the deep basin. This is why Zr is more important in runoff-derived tephra sediment than in the airfall tephra. Consequently, we attribute the increase in PC3 (representing Zr) to the presence of micropumice derived from the Mt Burney tephra layer.

Grain size analyses of pelagic sediments, as well as of flood-induced turbidites and dust storms facies, demonstrate that the percentage of clay and silt covaries and are anti-correlated with the sand percentage (Fig. 3b; Appendix C). However, silts are not correlated with clays or sands in micropumices-rich sediments. Statistical analyses on the divergence of silt and clay percentages for the whole PASADO sedimentary sequence (PASADO science team ongoing works) could thus become a proxy of micropumices at PTA.

5.4.2 Facies assemblage 2: Reworked tephra layer

In the light of the discovery of several fallen blocks of tephra material from a thick 40 cm tephra layer in the northwest canyon of the lake (Fig. 8), and situated about 15 meters above lake level, the presence of micropumices in sediments is suspected to be not only the result of wind transport, but also the consequence of precipitation runoff. Extreme precipitation runoff deposits were previously identified in the same PTA archive using the magnetic mineralogy of sediments and the stratigraphy (Lisé-Pronovost et al., 2014), one of which is a 22 cm thick reworked deposit composed of tephra layers and dated at 16 ka cal BP. The reworked tephra presented in this study reveals a facies assemblage typical of flood-induced turbidites (Arnaud et al., 2002; Giguet-Covex et al., 2012; Mulder and Alexander, 2001; Wilhelm et al., 2011) made of volcanoclastic particles (Fig. 5), of which the small thickness of the coarse facies at the bottom (about 2cm, facies 6 in Fig. 5) is consistent with a decrease in the duration and/or intensity of the floods in this interval. Similarly, Bertrand et al. (2014) showed that the redistribution of silty-sized micropumices to the deep basin of the Puyehue Lake (Chile, 40°S) is mainly driven by underflows or hyperpycnal flows. This would explain why reworked tephra layers are not directly on top of the airfall tephra layer. Moreover, in the 106.9-meter long PASADO composite sequence none of the thirteen tephra layers are directly followed by one of the eleven reworked tephra layers (data from Kliem et al., 2013a; Ohlendorf et al., 2011 and Wastegård et al., 2013). The sedimentary process could then be as follows: during the last Glacial period, the lake level was 21 m higher than the current level (Kliem et al., 2013a; b; Zolitschka et al., 2013). After an eruption, the ash plume passed over the lake, dispersing ashes all around. Because of the ease with which they can be transported by wind, micropumices around the lake were rapidly transported into the lake and elsewhere. Throughout the high lake level last Glacial period, the tephra layers were deposited when the lake covered a greater surface area. These tephra were subsequently covered by pelagic deposits. These high level terraces, including tephra, could therefore only be eroded during a subsequent low lake level. Precipitation runoff could then remobilized older consolidated tephras from several micropumices to entire blocks (Fig. 8). This hypothesis is supported by the integration of several micropumices within flood-induced turbidites (facies 1 in Fig. 5; 6) and not within dust storm event deposits (Fig. 5; Appendix B).

Interpretations of past atmospheric circulation derived from silt-sized particles, micropumices or acid insoluble ash over the Patagonian region and from lacustrine sedimentary sequence should be carefully conducted since their occurrence in the sedimentary record could be primarily controlled by rapid (precipitation events) or long time (fluctuation of lake level) hydrological processes, and require detailed thin-section examination.

5.5 Implications for paleoclimate reconstructions

Over ten years of paleoenvironmental and paleoclimate research at PTA were summarized in Zolitschka et al. (2013). These authors conclude that a high lake level stand (21 meters above the current lake level) was present during most of the last glacial period (51.2 to 17.3 ka cal BP), and that lake level dropped during the A2 and A1 intervals (Fig 2b). These lake level drops are inferred from peaks in total organic carbon (TOC) and biogenic silica (BSi) (Hahn et al., 2013) that point to higher paleoproductivity (Fig. 2b). Further support for a lake level drop during warm events is provided by Recasens et al. (2015), who reported higher diatom concentrations during A2 and A1. Diatom concentrations also peak during the AIM4 (Recasens et al., 2015) together with a moderate increase in BSi and TOC (Hahn et al., 2013), but no conclusion was drawn concerning PTA lake level during AIM4 since no significant warming in Antarctica is present during the Heinrich event 3 (H3) (Barbante et al., 2006). There is to date no comprehensive paleoclimate reconstruction of the AIM4 period in continental Patagonia. The only AIM4 records available for the southern South American region are marine sediment archives (Lamy et al., 2015; Caniupán et al., 2011). Grain size and geochemical analyses of marine sediment cores from southern Chilean continental slope at 53°S (core MD07-3128; position 52°39.57’S, 75°33.97’W) reveal a significant increase in terrigenous fine sand and sortable silt (Lamy et al., 2015), both proxies of near-bottom flow speed (McCave et al., 1996), critical amounts of Ice Rafted Debris (IRD) and peaks in the Alkenone STT (°C) (Caniupán et al., 2011) during all Antarctic isotope maxima of the last Glacial, including AIM4. This site is located less than 400 km away from PTA (Fig. 9). These authors provide thus evidences for increased near-bottom flow speed in the Cap Horn current (CHC) and the Antarctic circumpolar current (ACC) during these warm events. These interpretations are consistent with the bipolar seesaw mechanism on the Southern Ocean (Anderson et al., 2009; Barrows et al., 2007; Lamy et al., 2007, 2004), leading to surface water warming, enhanced upwelling, and stronger ACC caused by southward-shifted westerlies (Lamy et al., 2015). While paleoclimate data supports this scenario on the western side of the Andean Cordillera in the South Pacific sector of the Southern Ocean and the Drake Passage, the situation appears different on the eastern side where there is no evidence for upwelling in the South Atlantic sector of the Southern Ocean (Anderson et al., 2009) and no wind intensity change at 52°S during AIM4 (Lisé-Pronovost et al., 2015). In the meantime, a drastic input of dust in Antarctica (Barbante et al., 2006; Fig. 2) and in Scotia sea sediments (Weber et al., 2012; Fig. 2) is also recorded during AIM4.

The results presented here provide some hints of the mean climate state at 52°S in continental southeastern Patagonia. Indeed, a decrease in the thickness of runoff deposits (facies assemblage 1) and the occurrence of a series of wind bursts deposits (facies 2) together point to dustier conditions during AIM4. Other indicators at PTA, i.e. BSi, TOC (Hahn et al., 2013) and diatom concentration peaks (Recasens et al., 2015) are consistent with a lower lake level stand. Moreover, the runoff-driven micropumices detected in this study required lower lake levels to be mobilized, which further supports lower lake levels during AIM4. The increase in diatoms could also be interpreted as a consequence of the rapid dissolution of volcanic glass shards that bring additional silica to the water lake, which is a major nutrient source for building diatom frustules (Hickmann and Reasoner, 1994; De Klerck et al., 2008; Wutke et al., 2015). According to the PASADO age model, the sedimentation rate during AIM4 was about 1.375 $m.ka^{-1}$ (Kliem et al., 2013a). Micropumice-rich sediments (facies 8) are not characterized by reworked structures, in agreement with the sedimentological work of Kliem et al. (2013a) and with the careful analytical work on reworked tephras by Wutke et al. (2015). We thus proposed that the mobilization of micropumice by riverine processes, and during a low lake level stand, lasted about 600 years.

Our results improve environmental and climatic knowledge of the last glacial period derived from the multi-proxy record of PTA. They provide strong evidences of drier conditions than the average glacial condition at PTA during AIM4, and similar to the warm events A2 and A1, and is consistent with previous TOC, BSi and diatom analyses. Therefore, even during a slight increase in the atmospheric temperature in Antarctica (Barbante et al., 2006), this study suggest that the SWW contracted southward and imposed drier conditions at 52°S by blocking precipitation coming from the Atlantic Ocean, in a similar way to modern seasonal variations (Mayr et al., 2007b) (Fig. 9). The results indicate the SWW belt moved closer to PTA but did not reach 52°S in eastern Patagonia during AIM4 because the wind intensity proxy MDF_{IRM} (Fig. 2; Lisé-Pronovost et al, 2015) remained typical of the last glacial period, with lower average values and higher amplitude changes than during warmer periods such as the Holocene and the Antarctic warm events A1 and A2.

This study suggests a strongly non-symmetric SWW pattern over southern South America during AIM4 (Fig. 9). SWW may have been stronger at 52°S on the western side, deflecting stronger oceanic currents to the south of the continent, into the Drake Passage (Lamy et al., 2015) and to the Scotia Sea (Xiao et al., 2016). This interpretation is supported by recent multiproxy studies in Scotia Sea sediments from MIS8 (Xiao et al., 2016), which show that the k_{LF} is mainly controlled by detrital magnetic grains, originated from southeast Pacific and Patagonia continental margins, and carried by the Antarctic Circumpolar Current through the Drake passage. On the eastern side of the Andes however, data from LPA suggests the strong SWW were probably located slightly north of 52°S. Turbulent atmospheric flow situated just south of the SWW belt would induce highly variable wind directions and intensities in time and space, i.e. more gustiness. This is plausible since the AIM4 temperature change was small in Antarctica (Barbante et al., 2006), the SWW belt moved less than during the warmer events A2 and A1. The hypothesis of a SWW displacement proportional to the temperature gradient is consistent with the southward shift of the SWW belt during increased temperature (Mayewski et al., 2015) and reduced ice-sheet growth (Toggweiler, 2009; Venuti et al., 2011) and reduced sea-ice cover in Antarctica (Hudson and Hewitson, 2001).

The following scenario is suggested in order to explain the sharp magnetic susceptibility increase at 31.5 ka cal BP in the ICDP-PASADO record, and its discrepancy with wind intensity (Lisé-Pronovost et al., 2015). The drought conditions in the PTA area led to the activation of one or many new detrital sources rich in ferrimagnetic minerals. These more erodible and exposed sources provided the material for an increased atmospheric dust load that would account for the dust storm events recurrence and the magnetic susceptibility increase at PTA, as well as magnetic susceptibility peaks in the Southern Ocean (Weber et al., 2012) and dust deposition in Antarctica during the AIM4. Those high k_{LF} values in the PTA sediment archive were maintained until the onset of the deglaciation in southern Patagonia (17.3 ka cal BP), when atmospheric temperature increased, wind intensities steadily increased (Lisé-Pronovost et al., 2015) and pro-glacial lakes formed, acting as sediment traps in southeastern Patagonia (Sugden et al., 2009). The wind intensity reconstruction during AIM4 (Lisé-Pronovost et al., 2015) indicates a weaker displacement of the SWW compared to those during the A1 and A2. In this context, PTA would be close to the southern limit of the SWW belt, and susceptible to be influenced by easterly winds in case of slight northward displacement of the SWW.

6. Conclusions

This work provides the first detailed paleoclimate record of AIM4 (from 33 to 29 ka cal. BP), the latest Antarctic isotope maximum of the Last Glacial period, at 52°S in continental southeastern Patagonia. The high-resolution sedimentological and geochemical analyses reveal a decrease in the thickness of runoff deposits (facies assemblage 1 and probably 2) and a series of wind bursts deposits (facies 3), together pointing at drier conditions during AIM4. The inferred lake level drop would have induced the remobilization of micropumices during this period (facies 8). While results are in agreement with the paleoproductivity (Hahn et al., 2013; Recasens et al., 2015), paleowind (Lisé-Pronovost et al., 2015) and paleohydrological indicators at PTA (Hahn et al., 2014; Jouve et al., 2013; Kliem et al., 2013b; Lisé-Pronovost et al., 2014; Recasens et al., 2011; Schäbitz et al., 2013; Zhu et al., 2013), combining high-resolution sedimentological and geochemical analyses is the only way to differentiating runoff and wind-induced deposits. Whereas this high-resolution approach can hardly be applied to a long sedimentary sequence, this work also highlights the potential for using the divergence of silt and clay proportions as a rapid means for detecting changes in the origin of clastic grains deposited in lake sediments. This high-resolution work within AIM4 allows a short time frame observation of past climatic changes in southern South America during a period when temperature was rising in Antarctica, representing a good analogue for the current ongoing warming in Southern regions.

Acknowledgements

This research is supported by the International Continental Scientific Drilling Program (ICDP) in the framework of the “Potrok Aike Maar Lake Sediment Archive Drilling Project” (PASADO). Funding for drilling was provided by the ICDP, the German Science Foundation (DFG), the Swiss National Funds (SNF), the Natural Sciences and Engineering Research Council of Canada (NSERC), the Swedish Research Council - Vetenskapsrådet (VR) and the University of Bremen. For their invaluable help in field logistics and drilling we thank the staff of INTA Santa Cruz and Rio Dulce Catering as well as the Moreteau family and the DOSECC crew. This project was also made possible by an NSERC Discovery and a Canada Foundation for Innovation grants to P. Francus. We acknowledge the support of NSERC and the Canadian Meteorological and Oceanographical Society (CMOS) for graduate scholarships to A. Lisé-Pronovost. We also thank Quentin Simon for his relevant advices in the interpretation of the magnetic susceptibility signal.

References

Anderson, R.F., Ali, S., Bradtmiller, L.I., Nielsen, S.H.H., Fleisher, M.Q., Anderson, B.E., Burckle, L.H., 2009. Wind-Driven Upwelling in the Southern Ocean and the Deglacial Rise in Atmospheric CO2. Science 323, 1443–1448. doi:10.1126/science.1167441

Arnaud, F., Lignier, V., Revel, M., Desmet, M., Beck, C., Pourchet, M., Charlet, F., Trentesaux, A., Tribovillard, N., 2002. Flood and earthquake disturbance of 210Pb geochronology (Lake Anterne, NW Alps). Terra Nov. 14, 225–232. doi:10.1046/j.1365-3121.2002.00413.x

Barbante, C., Barnola, J.-M., Becagli, S., Beer, J., Bigler, M., Boutron, C., Blunier, T., Castellano, E., Cattani, O., Chappellaz, J., Dahl-Jensen, D., Debret, M., Delmonte, B., Dick, D., Falourd, S., Faria, S., Federer, U., Fischer, H., Freitag, J., Frenzel, A., Fritzsche, D., Fundel, F., Gabrielli, P., Gaspari, V., Gersonde, R., Graf, W., Grigoriev, D., Hamann, I., Hansson, M., Hoffmann, G., Hutterli, M.A., Huybrechts, P., Isaksson, E., Johnsen, S., Jouzel, J., Kaczmarska, M., Karlin, T., Kaufmann, P., Kipfstuhl, S., Kohno, M., Lambert, F., Lambrecht, A., Lambrecht, A., Landais, A., Lawer, G., Leuenberger, M., Littot, G., Loulergue, L., Lüthi, D., Maggi, V., Marino, F., Masson-Delmotte, V., Meyer, H., Miller, H., Mulvaney, R., Narcisi, B., Oerlemans, J., Oerter, H., Parrenin, F., Petit, J.-R., Raisbeck, G., Raynaud, D., Röthlisberger, R., Ruth, U., Rybak, O., Severi, M., Schmitt, J., Schwander, J., Siegenthaler, U., Siggaard-Andersen, M.-L., Spahni, R., Steffensen, J.P., Stenni, B., Stocker, T.F., Tison, J.-L., Traversi, R., Udisti, R., Valero-Delgado, F., van den Broeke, M.R., van de Wal, R.S.W., Wagenbach, D., Wegner, A., Weiler, K., Wilhelms, F., Winther, J.-G., Wolff, E., 2006. One-to-one coupling of glacial climate variability in Greenland and Antarctica. Nature 444, 195–198. doi:10.1038/nature05301

Barrows, T.T., Juggins, S., De Deckker, P., Calvo, E., Pelejero, C., 2007. Long-term sea surface temperature and climate change in the Australian-New Zealand region. Paleoceanography 22, PA2215. doi:10.1029/2006PA001328

Basile, I., Grousset, F.E., Revel, M., Petit, J.R., Biscaye, P.E., Barkov, N.I., 1997. Patagonian origin of glacial dust deposited in East Antarctica (Vostok and Dome C) during glacial stages 2, 4 and 6. Earth and Planetary Science Letters 146, 573–589. doi:10.1016/S0012-821X(96)00255-5

Bertrand, S., Daga, R., Bedert, R., Fontijn, K., 2014. Deposition of the 2011–2012 Cordón Caulle tephra (Chile, 40°S) in lake sediments: Implications for tephrochronology and volcanology. Journal of Geophysical Research: Earth Surface 119, 1–19. doi:10.1002/2014JF003321.Received

Blott, S.J., Pye, K., 2001. GRADISTAT: a grain size distribution and statistics package for the analysis of unconsolidated sediments. Earth Surface Processes and Landforms 26, 1237–1248. doi:10.1002/esp.261

Blunier, T., Brook, E.J., 2001. Timing of Millennial-Scale Climate Change in Antarctica and Greenland During the Last Glacial Period. Science 291, 109–112.

Blunier, T., Schwander, J., Stauffer, B., Stocker, T.F., Dallenbach, a., Indermuhle, a., Tschumi, J., Chappellaz, J., Raynaud, D., Barnola, J.-M., 1997. Timing of the Antarctic Cold Reversal and the atmospheric CO2 increase with respect to the Younger Dryas event. Geophysical Research Letters 24, 2683–2686. doi:10.1029/97GL02658

Caniupán, M., Lamy, F., Lange, C.B., Kaiser, J., Arz, H., Kilian, R., Baeza Urrea, O., Aracena, C., Hebbeln, D., Kissel, C., Laj, C., Mollenhauer, G., Tiedemann, R., 2011. Millennial-scale sea surface temperature and Patagonian Ice Sheet changes off southernmost Chile (53°S) over the past ∼60 kyr. Paleoceanography 26, PA3221. doi:10.1029/2010PA002049

Croudace, I.W., Rindby, A., Rothwell, R.G., 2006. ITRAX: description and evaluation of a new multi-function X-ray core scanner. The Geological Society of London, Spec. Publ. 267, 51–63. doi:10.1144/GSL.SP.2006.267.01.04

D’Orazio, M., Agostini, S., Mazzarini, F., Innocenti, F., Manetti, P., Haller, M.J., Lahsen A., 2000. The Pali Aike Volcanic Field, Patagonia: slab-window magmatism near the tip of South America. Tectonophysics 321: 407-427.

d’Orgeville, M., Sijp, W.P., England, M.H., Meissner, K.J., 2010. On the control of glacial-interglacial atmospheric CO2 variations by the Southern Hemisphere westerlies. Geophysical Research Letters 37, L21703. doi:10.1029/2010GL045261

De Keyser, T.L., 1999. Digital Scanning of Thin Sections and Peels. J. Sediment. Res. 69, 962-964.

De Klerck, P., Janke,W., Kühn, P., Theuerkauf, M., 2008. Environmental impact of the Laacher See eruption at large distance from the volcano: integrated palaeoecological studies from Vorpommern (NE Germany). Palaeogeography Palaeoclimatology Palaeoecology 270, 196-214.

Delmonte, B., Baroni, C., Andersson, P.S., Schoberg, H., Hansson, M., Aciego, S., Petit, J.-R., Albani, S., Mazzola, C., Maggi, V., Frezzotti, M., 2010. Aeolian dust in the Talos Dome ice core (East Antarctica, Pacific/Ross Sea sector): Victoria Land versus remote sources over the last two climate cycles. Journal of Quaternary Science 25, 1327–1337. doi:10.1002/jqs.1418

Delmonte, B., Petit, J.R., Andersen, K.K., Basile-Doelsch, I., Maggi, V., Ya Lipenkov, V., 2004. Dust size evidence for opposite regional atmospheric circulation changes over east Antarctica during the last climatic transition. Climate Dynamics 23, 427-438. doi:10.1007/s00382-004-0450-9

Endlicher, W., 1993. Klimatische Aspekte der Weidedegradation in Ost-Patagonien. Ralph Jätzold. Geogr. Gesellschaft Trier, Trier 91–103.

Folk, R.L., Ward, W.C., 1957. Brazos River Bar: A Study in the Significance of Grain Size Parameters. Journal of Sedimentary Research 27, 3-26.

Francus, P., 1998. An image-analysis technique to measure grain-size variation in thin sections of soft clastic sediments. Sedimentary Geology 121, 289–298. doi:10.1016/S0037-0738(98)00078-5

Francus, P., Asikainen, C. a., 2001. Sub-sampling unconsolidated sediments: A solution for the preparation of undisturbed thin-sections from clay-rich sediments. Journal of Paleolimnology 26, 323–326. doi:10.1023/A:1017572602692

Francus, P., Bradley, R.S., Abbott, M.B., Patridge, W., Keiming, F., 2002. Paleoclimate studies of minerogenic sediments using annually resolved textural parameters. Geophysical Research Letters 29, 1998–2001. doi:10.1029/2002GL015082

Francus, P., Karabanov, E., 2000. A computer-assisted thin-section study of Lake Baikal sediments: a tool for understanding sedimentary processes and deciphering their climatic signal. International Journal of Earth Sciences 89, 260–267. doi:10.1007/s005319900064

Francus, P., Nobert, P., 2007. An integrated computer system to acquire, process, measure and store images of laminated sediments. 4th Int. limnogeology Congr. Barcelona.

Gaiero, D.M., 2007. Dust provenance in Antarctic ice during glacial periods: From where in southern

South America? Geophysical Research Letters 34, L17707. doi:10.1029/2007GL030520

Giguet-Covex, C., Arnaud, F., Enters, D., Poulenard, J., Millet, L., Francus, P., David, F., Rey, P.J., Wilhelm, B., Delannoy, J.J., 2012. Frequency and intensity of high-altitude floods over the last 3.5ka in northwestern French Alps (Lake Anterne). Quaternary Research 77, 12–22. doi:10.1016/j.yqres.2011.11.003

Gilbert, R., Crookshanks, S., Hodder, K.R., Spagnol, J., Stull, R.B., 2006. The Record of an Extreme Flood in the Sediments of Montane Lillooet Lake, British Columbia: Implications for Paleoenvironmental Assessment. Journal of Paleolimnology 35, 737–745. doi:10.1007/s10933-005-5152-8

González, L., Rial, P., 2004. Guía geográfica interactiva de Santa Cruz, in: INTA-CAP-UNPA. Rio Gallegos, Argentina.

Haberzettl, T., Anselmetti, F.S., Bowen, S.W., Fey, M., Mayr, C., Zolitschka, B., Ariztegui, D., Mauz, B., Ohlendorf, C., Kastner, S., Lücke, A., Schäbitz, F., Wille, M., 2009. Late Pleistocene dust deposition in the Patagonian steppe - extending and refining the paleoenvironmental and tephrochronological record from Laguna Potrok Aike back to 55 ka. Quaternary Science Reviews 28, 2927–2939. doi:10.1016/j.quascirev.2009.07.021

Haberzettl, T., Kück, B., Wulf, S., Anselmetti, F., Ariztegui, D., Corbella, H., Fey, M., Janssen, S., Lücke, A., Mayr, C., Ohlendorf, C., Schäbitz, F., Schleser, G.H., Wille, M., Zolitschka, B., 2008. Hydrological variability in southeastern Patagonia and explosive volcanic activity in the southern Andean Cordillera during Oxygen Isotope Stage 3 and the Holocene inferred from lake sediments of Laguna Potrok Aike, Argentina. Palaeogeography Palaeoclimatology Palaeoecology 259, 213–229. doi:10.1016/j.palaeo.2007.10.008

Haberzettl, T., Corbella, H., Fey, M., Janssen, S., Lucke, A., Mayr, C., Ohlendorf, C., Schabitz, F., Schleser, G.H., Wille, M., Wulf, S., Zolitschka, B., 2007. Lateglacial and Holocene wet--dry cycles in southern Patagonia: chronology, sedimentology and geochemistry of a lacustrine record from Laguna Potrok Aike, Argentina. The Holocene 17, 297–310. doi:10.1177/0959683607076437

Haberzettl, T., Fey, M., Lücke, A., Maidana, N., Mayr, C., Ohlendorf, C., Schäbitz, F., Schleser, G.H., Wille, M., Zolitschka, B., 2005. Climatically induced lake level changes during the last two millennia as reflected in sediments of Laguna Potrok Aike, southern Patagonia (Santa Cruz, Argentina). Journal of Paleolimnology 33, 283–302. doi:10.1007/s10933-004-5331-z

Hahn, A., Kliem, P., Oehlerich, M., Ohlendorf, C., Zolitschka, B., Team, P.S., 2014. Elemental composition of the Laguna Potrok Aike sediment sequence reveals paleoclimatic changes over the past 51 ka in southern Patagonia, Argentina. Journal of Paleolimnology 52, 349–366. doi:10.1007/s10933-014-9798-y

Hahn, A., Kliem, P., Ohlendorf, C., Zolitschka, B., Rosén, P., 2013. Climate induced changes as registered in inorganic and organic sediment components from Laguna Potrok Aike (Argentina) during the past 51 ka. Quaternary Science Reviews 71, 154–166. doi:10.1016/j.quascirev.2012.09.015

Hickmann, M., Reasoner, M., 1994. Diatom responses to late Quaternary vegetation and climate change, and to deposition of two tephras in an alpine and subalpine lake in Yoho National Park, British Colombia. Journal of Paleolimnology 11, 173-188. doi: 10.1007/BF00686864

Hodgson, D. a., Sime, L.C., 2010. Palaeoclimate Southern westerlies and CO2. Nature Geoscience 3, 666–667. doi:10.1038/ngeo970

Hudson, D.A., Hewitson, C., 2001. The atmospheric response to a reduction in summer Antarctic sea-ice extent. Climate Research 16, 79–99. doi:10.3354/cr016079

Jouve, G., Francus, P., Lamoureux, S., Provencher-Nolet, L., Hahn, A., Haberzettl, T., Fortin, D., Nuttin, L., 2013. Microsedimentological characterization using image analysis and µ-XRF as indicators of sedimentary processes and climate changes during Lateglacial at Laguna Potrok Aike, Santa Cruz, Argentina. Quaternary Science Reviews 71, 191–204. doi:10.1016/j.quascirev.2012.06.003

Kaiser, J., Lamy, F., Hebbeln, D., 2005. A 70-kyr sea surface temperature record off southern Chile (Ocean Drilling Program Site 1233). Paleoceanography 20, PA4009. doi:10.1029/2005PA001146

Kastner, S., Ohlendorf, C., Haberzettl, T., Lücke, A., Mayr, C., Maidana, N.I., Schäbitz, F., Zolitschka, B., 2010. Southern hemispheric westerlies control the spatial distribution of modern sediments in Laguna Potrok Aike, Argentina. Journal of Paleolimnology 44, 887–902. doi:10.1007/s10933-010-9462-0

Kliem, P., Buylaert, J.P., Hahn, A., Mayr, C., Murray, A.S., Ohlendorf, C., Veres, D., Wastegård, S., Zolitschka, B., 2013. Magnitude, geomorphologic response and climate links of lake level oscillations at Laguna Potrok Aike, Patagonian steppe (Argentina). Quaternary Science Reviews 71, 131–146. doi:10.1016/j.quascirev.2012.08.023

Kliem, P., Enters, D., Hahn, A., Ohlendorf, C., Lisé-Pronovost, A., St-Onge, G., Wastegård, S., Zolitschka, B., 2013. Lithology, radiocarbon chronology and sedimentological interpretation of the lacustrine record from Laguna Potrok Aike, southern Patagonia. Quaternary Science Reviews 71, 54–69. doi:10.1016/j.quascirev.2012.07.019

Kohfeld, K.E., Graham, R.M., de Boer, A.M., Sime, L.C., Wolff, E.W., Le Quéré, C., Bopp, L., 2013. Southern Hemisphere westerly wind changes during the Last Glacial Maximum: paleo-data synthesis. Quaternary Science Reviews 68, 76–95. doi:10.1016/j.quascirev.2013.01.017

Krumbein, W.C., Sloss, S.L., 1963. Stratigraphy and Sedimentation, 2nd edition. ed. Freeman, San Francisco.

Kuhlbrodt, T., Griesel, A., Montoya, M., Levermann, A., Hofmann, M., Rahmstorf, S., 2007. On the driving processes of the Atlantic meridional overturning circulation. Reviews of Geophysics 45, RG2001. doi:10.1029/2004RG000166

Lamoureux, S., Bollmann, J., 2004. Image acquisition, in: Francus, P. (Ed.), Image Analysis, Sediments and Paleoenvironments. Dordrecht, pp. 11–34. doi:10.1007/1-4020-2122-4_2

Lamoureux, S.F., 1994. Embedding unfrozen lake sediments for thin section preparation. Journal of Paleolimnology 10, 141–146. doi:10.1007/BF00682510

Lamy, F., Arz, H.W., Kilian, R., Lange, C.B., Wengler, M., Kaiser, J., 2015. Glacial reduction and millennial - scale variations in Drake Passage throughflow. Proceedings of the National Academy of Science of the United States of America, PNAS 112, 13496–13501 doi:10.1073/pnas.1509203112

Lamy, F., Kaiser, J., Arz, H.W., Hebbeln, D., Ninnemann, U., Timm, O., Timmermann, A., Toggweiler, J.R., 2007. Modulation of the bipolar seesaw in the Southeast Pacific during

Termination 1. Earth and Planetary Science Letters 259, 400–413. doi:10.1016/j.epsl.2007.04.040

Lamy, F., Kaiser, J., Ninnemann, U., Hebbeln, D., Arz, H.W., Stoner, J., 2004. Antarctic Timing of Surface Water Changes off Chile and Patagonian Ice Sheet Response. Science 304, 1959–1962. doi:10.1126/science.1097863

Lamy, F., Kilian, R., Arz, H.W., Francois, J.-P., Kaiser, J., Prange, M., Steinke, T., 2010. Holocene changes in the position and intensity of the southern westerly wind belt. Nature Geoscience 3, 695–699. doi:10.1038/ngeo959

Last, W.M., Smol, J.P. (Eds.), 2002. Tracking Environmental Change Using Lake Sediments, Developments in Paleoenvironmental Research. Kluwer Academic Publishers, Dordrecht. doi:10.1007/0-306-47670-3

Ledru, M.-P., Rousseau, D.-D., Cruz, F.W., Riccomini, C., Karmann, I., Martin, L., 2005. Paleoclimate changes during the last 100,000 yr from a record in the Brazilian Atlantic rainforest region and interhemispheric comparison. Quaternary Research 64, 444–450. doi:10.1016/j.yqres.2005.08.006

Lisé-Pronovost, A., St-Onge, G., Gogorza, C., Haberzettl, T., Jouve, G., Francus, P., Ohlendorf, C., Gebhardt, C., Zolitschka, B., 2015. Rock-magnetic proxies of wind intensity and dust since 51,200 cal BP from lacustrine sediments of Laguna Potrok Aike, southeastern Patagonia. Earth and Planetary Science Letters 411, 72–86. doi:10.1016/j.epsl.2014.11.007

Lisé-Pronovost, A., St-Onge, G., Gogorza, C., Haberzettl, T., Preda, M., Kliem, P., Francus, P., Zolitschka, B., 2013. High-resolution paleomagnetic secular variations and relative paleointensity since the Late Pleistocene in southern South America. Quaternary Science Reviews 71, 91–108. doi:10.1016/j.quascirev.2012.05.012

Lisé-Pronovost, A., St-Onge, G., Gogorza, C., Jouve, G., Francus, P., Zolitschka, B., 2014. Rock-magnetic signature of precipitation and extreme runoff events in south-eastern Patagonia since 51,200calBP from the sediments of Laguna Potrok Aike. Quaternary Science Reviews 98, 110–125. doi:10.1016/j.quascirev.2014.05.029

Mazzarini, F., D’Orazio, M., 2003. Spatial distribution of cones and satellite-detected lineaments in the Pali Aike Volcanic Field (southernmost Patagonia): insights into the tectonic setting of a Neogene rift system. Journal of Volcanology and Geothermal Research 125: 291-305.

Matter, A., Tucker, M.E. (Eds.), 1978. Modern and Ancient Lake Sediments. Blackwell Publishing Ltd., Oxford, UK. doi:10.1002/9781444303698

Mayewski, P.A., Bracegirdle, T., Goodwin, I., Schneider, D., Bertler, N.A.N., Birkel, S., Carleton, A., England, M.H., Kang, J.-H., Khan, A., Russel, J., Turner, J., Velicogna, I., 2015. Potential for Southern Hemisphere climate surprises. Journal of Quaternary Science 30, 391–395. doi:10.1002/jqs.2794

Mayr, C., Lücke, A., Stichler, W., Trimborn, P., Ercolano, B., Oliva, G., Ohlendorf, C., Soto, J., Fey, M., Haberzettl, T., Janssen, S., Schäbitz, F., Schleser, G.H., Wille, M., Zolitschka, B., 2007a. Precipitation origin and evaporation of lakes in semi-arid Patagonia (Argentina) inferred from stable isotopes (δ18O, δ2H). Journal of Hydrology 334, 53–63. doi:10.1016/j.jhydrol.2006.09.025

Mayr, C., Wille, M., Haberzettl, T., Fey, M., Janssen, S., Lücke, A., Ohlendorf, C., Oliva, G., Schäbitz, F., Schleser, G.H., Zolitschka, B., 2007b. Holocene variability of the Southern Hemisphere westerlies in Argentinean Patagonia (52°S). Quaternary Science Reviews 26, 579–584. doi:10.1016/j.quascirev.2006.11.013

McCave, I.N., Manighetti, B., Robinson, S.G., 1996. Sortable silt and fine sediment size/composition slicing: parameters for palaeocurrent speed and palaeoceanography. I. N. McCave, B. Manighetti, S. G. Robinson. 1996. Sortable silt fine sediment size/composition slicing parameters palaeocurrent speed palaeoceanography. Oceanographic Literature Review 43 45. 1, 45.

McCulloch, R.D., Bentley, M.J., Purves, R.S., Hulton, N.R.J., Sugden, D.E., Clapperton, C.M., 2000. Climatic inferences from glacial and palaeoecological evidence at the last glacial termination, southern South America. Journal of Quaternary Science 15, 409–417. doi:10.1002/1099-1417(200005)15:4<409::AID-JQS539>3.0.CO;2-#

McDonald, D.M., Lamoureux, S.F., 2009. Hydroclimatic and channel snowpack controls over suspended sediment and grain size transport in a High Arctic catchment. Earth Surface Processes and Landforms 34, 424–436. doi:10.1002/esp.1751

Mcglone, M.S., Turney, C.S.M., Wilmshurst, J.M., Renwick, J., Pahnke, K., 2010. Divergent trends in land and ocean temperature in the Southern Ocean over the past 18,000 years. Nature Geoscience 3, 622–626. doi:10.1038/ngeo931

Menviel, L., Timmermann, A., Mouchet, A., Timm, O., 2008. Climate and marine carbon cycle response to changes in the strength of the Southern Hemispheric westerlies. Paleoceanography 23, PA4201. doi:10.1029/2008PA001604

Mulder, T., Chapron, E., 2011. Flood Deposits in Continental and Marine Environments: Character and Significance. In R. M. Slatt and C. Zavala, eds., Sediment transfer from shelf to deep water-revisting the delivery system: AAPG Studies in Geology, 61, 1–30. doi:10.1306/13271348St613436

Mulder, T., Syvitski, J.P.M., Migeon, S., Faugères, J.-C., Savoye, B., 2003. Marine hyperpycnal flows: initiation, behavior and related deposits. A review. Marine and Petroleum Geology 20, 861–882. doi:10.1016/j.marpetgeo.2003.01.003

Mulder, T., Alexander, J., 2001. The physical character of subaqueous sedimentary density flows and their deposits. Sedimentology 48, 269-299.

Ohlendorf, C., Fey, M., Gebhardt, C., Haberzettl, T., Lücke, A., Mayr, C., Schäbitz, F., Wille, M., Zolitschka, B., 2013. Mechanisms of lake-level change at Laguna Potrok Aike (Argentina) – insights from hydrological balance calculations. Quaternary Science Reviews 71, 27–45. doi:10.1016/j.quascirev.2012.10.040

Ohlendorf, C., Gebhardt, C., Hahn, A., Kliem, P., Zolitschka, B., 2011. The PASADO core processing strategy - A proposed new protocol for sediment core treatment in multidisciplinary lake drilling projects. Sedimentary Geology 239, 104–115. doi:10.1016/j.sedgeo.2011.06.007

Petit, J.R., Jouzel, J., Raynaud, D., Barkov, N.I., Barnola, J.-M., Basile, I., Bender, M., Chappellaz, J., Davis, M., Delaygue, G., Delmotte, M., Kotlyakov, V.M., Legrand, M., Lipenkov, V.Y., Lorius, C., PEpin, L., Ritz, C., Saltzman, E., Stievenard, M., 1999. Climate and atmospheric history of the past 420,000 years from the Vostok ice core, Antarctica. Nature 399, 429–436. doi:10.1038/20859

Pollock, E.W., Bush, A.B.G., 2013. Atmospheric simulations of southern South America's climate since the Last Glacial maximum. Quaternary Science Reviews 71, 219–228. doi:10.1016/j.quascirev.2012.09.019

Recasens, C., Ariztegui, D., Gebhardt, C., Gogorza, C., Haberzettl, T., Hahn, A., Kliem, P., Lise-Pronovost, A., Lucke, A., Maidana, N., Mayr, C., Ohlendorf, C., Schabitz, F., St-Onge, G., Wille, M., Zolitschka, B., Team, S., 2011. New insights into paleoenvironmental changes in Laguna Potrok Aike, southern Patagonia, since the Late Pleistocene: The PASADO multiproxy record. The Holocene 22, 1323–1335. doi:10.1177/0959683611429833

Recasens, C., Ariztegui, D., Maidana, N.I., Zolitschka, B., 2015. Diatoms as indicators of hydrological and climatic changes in Laguna Potrok Aike (Patagonia) since the Late Pleistocene. Palaeogeography Palaeoclimatology Palaeoecology 417, 309–319. doi:10.1016/j.palaeo.2014.09.021

Šabacká, M., Priscu, J.C., Basagic, H.J., Fountain, A.G., Wall, D.H., Virginia, R. a., Greenwood, M.C., 2012. Aeolian flux of biotic and abiotic material in Taylor Valley, Antarctica. Geomorphology 155-156, 102–111. doi:10.1016/j.geomorph.2011.12.009

Sapkota, A., Cheburkin, A.K., Bonani, G., Shotyk, W., 2007. Six millennia of atmospheric dust deposition in southern South America (Isla Navarino, Chile). The Holocene 17, 561–572. 10.1177/0959683607078981. doi:10.1177/0959683607078981

Schäbitz, F., Wille, M., Francois, J.-P., Haberzettl, T., Quintana, F., Mayr, C., Lücke, A., Ohlendorf, C., Mancini, V., Paez, M.M., Prieto, A.R., Zolitschka, B., 2013. Reconstruction of palaeoprecipitation based on pollen transfer functions – the record of the last 16 ka from Laguna Potrok Aike, southern Patagonia. Quaternary Science Reviews 71, 175–190. doi:10.1016/j.quascirev.2012.12.006

Schneider, C., Glaser, M., Kilian, R., Santana, A., Butorovic, N., Casassa, G., 2003. Weather Observations Across the Southern Andes at 53°S. Physical Geography 24, 97–119. doi:10.2747/0272-3646.24.2.97

Shiki, T., Kumon, F., Inouchi, Y., Kontani, Y., Sakamoto, T., Tateishi, M., Matsubara, H., Fukuyama, K., 2000. Sedimentary features of the seismo-turbidites, Lake Biwa, Japan. Sedimentary Geology

135, 37–50. doi:10.1016/S0037-0738(00)00061-0

Sijp, W.P., England, M.H., 2009. Southern Hemisphere Westerly Wind Control over the Ocean's Thermohaline Circulation. Journal of Climate 22, 1277-1286. doi:10.1175/2008JCLI2310.1

Skewes, M.A., 1978. Geologia, petrologia, quimismo y origen de los volcanes del area de Pali-Aike, Magallanes, Chile. Anales del Instituto de la Patagonia 9, 95-106.

Sperazza, M., Moore, J.N., and Hendrix, M.S., 2004. High-resolution particle size analysis of naturally occurring very fine-grained sediment through laser diffractometry, Journal of Sedimentary Research 74, 736-743.

Sugden, D.E., McCulloch, R.D., Bory, A.J.-M., Hein, A.S., 2009. Influence of Patagonian glaciers on Antarctic dust deposition during the last glacial period. Nature Geoscience 2, 281–285. doi:10.1038/ngeo474

Toggweiler, J.R., 2009. Climate change. Shifting westerlies. Science 323, 1434–5. doi:10.1126/science.1169823

Toggweiler, J.R., Russell, J.L., Carson, S.R., 2006. Midlatitude westerlies, atmospheric CO 2 , and climate change during the ice ages. Paleoceanography 21, PA2005. doi:10.1029/2005PA001154

Toggweiler, J.R., Samuels, B., 1995. Effect of drake passage on the global thermohaline circulation. Deep Sea Research Part I: Oceanographic Research Papers 42, 477–500. doi:10.1016/0967-0637(95)00012-U

Tschumi, T., Joos, F., Parekh, P., 2008. How important are Southern Hemisphere wind changes for low glacial carbon dioxide? A model study. Paleoceanography 23, PA4208. doi:10.1029/2008PA001592

Vanneste, H., De Vleeschouwer, F., Martínez-Cortizas, A., von Scheffer, C., Piotrowska, N., Coronato, A., Le Roux, G. 2015. Late-glacial elevated dust deposition linked to westerly wind shifts in southern South America. Nature Scientific Report 5, 11670; doi:10.1038/srep11670.

Venuti, A., Florindo, F., Caburlotto, A., Hounslow, M.W., Hillenbrand, C.-D., Strada, E., Talarico, F.M., Cavallo, A., 2011. Late Quaternary sediments from deep-sea sediment drifts on the Antarctic Peninsula Pacific margin: Climatic control on provenance of minerals. Journal of Geophysical Research: Solid Earth 116, B06104. doi:10.1029/2010JB007952

Wastegård, S., Veres, D., Kliem, P., Hahn, A., Ohlendorf, C., Zolitschka, B., 2013. Towards a late Quaternary tephrochronological framework for the southernmost part of South America – the Laguna Potrok Aike tephra record. Quaternary Science Reviews 71, 81–90. doi:10.1016/j.quascirev.2012.10.019

Weber, M.E., Kuhn, G., Sprenk, D., Rolf, C., Ohlwein, C., Ricken, W., 2012. Dust transport from Patagonia to Antarctica – A new stratigraphic approach from the Scotia Sea and its implications for the last glacial cycle. Quaternary Science Reviews 36, 177–188. doi:10.1016/j.quascirev.2012.01.016

Wilhelm, B., Arnaud, F., Enters, D., Allignol, F., Legaz, A., Magand, O., Revillon, S., Giguet-Covex, C., Malet, E., 2011. Does global warming favour the occurrence of extreme floods in European Alps? First evidences from a NW Alps proglacial lake sediment record. Climatic Change 113, 563–581. doi:10.1007/s10584-011-0376-2

Wilhelm, B., Arnaud, F., Sabatier, P., Magand, O., Chapron, E., Courp, T., Tachikawa, K., Fanget, B., Malet, E., Pignol, C., Bard, E., Delannoy, J.J., 2013. Palaeoflood activity and climate change over the last 1400 years recorded by lake sediments in the north-west European Alps. Journal of Quaternary Science 28, 189–199. doi:10.1002/jqs.2609

Wilhelm, B., Sabatier, P., Arnaud, F., 2015. Is a regional flood signal reproducible from lake sediments? Sedimentology 62, 1103–1117. doi:10.1111/sed.12180

Wille M, Maidana NI, Schäbitz F, Fey M, Haberzettl T, Janssen S, Lücke A, Mayr C, Ohlendorf C, Schleser GH, Zolitschka B (2007) Vegetation and climate dynamics in southern South America: the microfossil record of Laguna Potrok Aike, Santa Cruz, Argentina. Review of Palaeobotany and Palynology 146:234–246

Wutke, K., Wulf, S., Tomlinson, E.L., Hardiman, M., Dulski, P., Luterbacher, J., Brauer, A., 2015. Geochemical properties and environmental impacts of seven Campanian tephra layers deposited between 60 and 38 ka BP in the varved lake sediments of Lago Grande di Monticchio, southern Italy. Quaternary Science Reviews 118, 67-83.

Xiao, W., Frederichs, T., Gersonde, R., Kuhn, G., Esper, O., Zhang, X., 2016. Constraining the dating of late Quaternary marine sediment records from the Scotia Sea (Southern Ocean). Quaternary

Geochronology 31, 97–118. doi:10.1016/j.quageo.2015.11.003

Zhu, J., Lücke, A., Wissel, H., Müller, D., Mayr, C., Ohlendorf, C., Zolitschka, B., 2013. The last Glacial-Interglacial transition in Patagonia, Argentina: The stable isotope record of bulk sedimentary organic matter from Laguna Potrok Aike. Quaternary Science Reviews 71, 205–218. doi:10.1016/j.quascirev.2012.05.025

Zolitschka, B., Anselmetti, F., Ariztegui, D., Corbella, H., Francus, P., Lücke, a., Maidana, N.I., Ohlendorf, C., Schäbitz, F., Wastegård, S., 2013. Environment and climate of the last 51,000years - new insights from the Potrok Aike maar lake Sediment Archive Drilling prOject (PASADO). Quaternary Science Reviews 71, 1–12. doi:10.1016/j.quascirev.2012.11.024

Zolitschka, B., Anselmetti, F., Ariztegui, D., Corbella, H., Francus, P., Ohlendorf, C., Schäbitz, F., 2009. The laguna potrok aike scientiic drilling project PASADO (ICDP expedition 5022). Scientific Drilling Journal 29–34. doi:10.2204/iodp.sd.8.04.2009

Zolitschka, B., Schäbitz, F., Lücke, A., Corbella, H., Ercolano, B., Fey, M., Haberzettl, T., Janssen, S., Maidana, N., Mayr, C., Ohlendorf, C., Oliva, G., Paez, M.M., Schleser, G.H., Soto, J., Tiberi, P., Wille, M., 2006. Crater lakes of the Pali Aike Volcanic Field as key sites for paleoclimatic and paleoecological reconstructions in southern Patagonia, Argentina. Journal of South American Earth Sciences 21, 294–309. doi:10.1016/j.jsames.2006.04.001

http://portal.gplates.org/cesium/?view=topo15

Table, Figures and Appendix captions

Table 1: Representation quality of the variables (variables cosine-squared) and their contribution to the construction of the components, derived from the principal component analysis conducted on µ-XRF data for the sedimentary interval between 40.62 to 37.90 m cd.

Figure 1: Location of Laguna Potrok Aike in southern Patagonia (blue circle on inset map of South America). Aerial photograph of the immediate catchment area of Laguna Potrok Aike (kindly provided by Hugo Corbella) and bathymetric map of the lake with indicated coring site 5022-2. Red dots indicate the positions of piston cores (modified from Ohlendorf et al., 2011). Paleoshorelines surrounding the lake are indicated with the black arrow. Red stars show locations of fallen tephra layers in western canyons (this study and Kliem et al., 2013b).

Figure 2: a: Stratigraphy (in meter composite depth, m cd) and age model of the PASADO sedimentary record (site 2) (Kliem et al. 2013a). Units are indicated on the left side: Unit A: Laminated silts prevail, with a relatively high amount of carbonate crystals. Unit B: Dominance of laminated silts intercalated with thin fine sand and coarse silt layers: normal graded units and ball and pillow structures occur. Few carbonate crystals occur. Unit C-1: Dominance of laminated silts intercalated with thin fine sand and coarse silt layers. Normal graded units and ball and pillow structures occur. Unit C-2: Dominance of normally graded beds and ball and pillow structures among laminated silts intercalated with thin fine sands and coarse silt layers. b: Green curves: percentage of biogenic silica (BSi) (Hahn et al., 2013) and concentration of diatoms valves in sediment (million valves gr^{-1} of dry sediment) (Recasens et al., 2014), both proxies of paleoproductivity. Black and grey curves (left): median destructive field of the isothermal remanent magnetization (MDF_{IRM}), a proxy of wind intensity at PTA (Lisé-Pronovost et al., 2015). Low field magnetic susceptibility (k_{LF}) in PTA sediments as

proxy of gustiness and/or dust availability (Lisé-Pronovost et al., 2015). Black and grey curves (right): magnetic susceptibility in Scotia Sea (k_{LF}) and dust mass (p.p.b.) in EPICA Dome C (Antarctica), as proxies of dust from Patagonia during the Last Glacial. Black vertical dotted lines show average values. Red vertical dotted lines show average values before and after 31.5 ka cal. BP for the MDF_{IRM}, K_{LF} (PTA and Scotia Sea) and dust mass in Antarctica. The interval covering the AIM4, A1, A2, A3 (Barbante et al., 2006) are represented by the yellow rectangles. Black arrow on the right side indicates the occurrence of the first dust storm event (DSE) for the interval under study.

Figure 3: a: Core images of the AIM4 interval (image from Ohlendorf et al., 2011), with the position of the radiocarbon date, in ka cal. BP. All results are plotted in meter composite depth (m cd; left side). b: Laser diffraction grain size analysis of 206 samples plotted in percentage with 2 sigma errors bars. c: Principal Component Analysis of the first (PCA1, driven by Fe, Ti and K), the second (PC2, driven by Ca, Si and Sr) and the third (PCA3, driven by Zr) principal components. Detailed curves of each element are available in Appendix A.

Figure 4: a: natural and cross-polarized light of thin sections for FIT 1, DSE 1 and the Mount Burney tephra layer with depth in m cd. b: Calcium and PC2 values plotted with depth. c: laser diffraction grain size plotted with depth.

Figure 5: Facies, microfacies and image analyses of the facies assemblage 1 (flood-induced turbidites), dust storm, pelagic, tephra, facies assemblage 2 (reworked tephra) and micropumices-rich sedimentary facies. Left side: cross-polarized or natural light image of thin sections, with the position of BSE images (white numbers and arrows) used to perform image

analysis grain size (right and below). Right side: BSE and binary images of microfacies most representative of each facies, and used to calculate the grain size of clastic grains.

Figure 6: a: core images of flood-induced turbidite events a to d during the AIM4. The flood-intensity is indicated with a bold and black arrow. b: Natural light image of microfacies at the bottom of the flood. Note the presence of macrophytes in each microfacies. c: laser diffraction grain size results of each flood event showing the fining upwards.

Figure 7: Backscattered and binary images of microfacies for the background (sedimentary deposit under mean climate state conditions) and for each dust storm event (DSE). Image analysis grain size highlights the increased rate of sand during DSE.

Figure 8: Top: Photographs of the shoreline enriched by macrophytes. Middle: photographs of the canyon in the northwest part of the lake showing several collapsed blocks of tephra. Bottom: photography of a gust of wind coming from the West. All photographs were taken by Guillaume Jouve during a field campaign in February 2010.

Figure 9: Northern and southern position and extension of the SWW belt during the Glacial, the AIM4 and the A1, A2 warm events, as inferred from this work and the work of Hodgson and Sime (2010), Lamy et al. (2010) and McGlone et al. (2010). World topography data are available at http://portal.gplates.org/cesium/?view=topo15.

Appendix A: Elemental µ-XRF profiles along the interval under study for Fe, Ti, K, Si, Ca, Sr and Zr reported in peak area, and results of the PCA analysis also available in Figure 3c.

Appendix B: a: core images from the PASADO sequence (Ohlendorf et al., 2011), with the position of Flood-Induced Turbidites c and d (FITc and d), and dust storm events (DSE 1-7; Fig. 3). b: cross-polarized light images of thin sections of the seven dust storm events detected in the interval, showing matrix-supported and non-erosive base structures.

Appendix C: Scatter plots of the different grain-size fraction within the interval between 40.62 - 38.7 m cd (black points, below Mount Burney tephra) and 38.7 – 37.9 m cd (grey points, above Mount Burney tephra). a. Clays versus silts, b. clays versus sands and c. silts versus sands plots obtained from laser diffraction grain size data. Blue dotted lines and equations are for samples below Mount Burney tephra, while red lines and equations are for samples above Mount Burney tephra.

Appendix D: Detailed statistics on PCA analyses conducted on μ-XRF data

Table 1

	F1 = PC1 (25.2%)	F2 = PC2 (16.3%)	F3 = PC3 (11.3%)	F4	F5
Si	0.027	**0.551**	0.092	0.011	0.000
K	**0.470**	0.182	0.015	0.055	0.005
Ca	0.019	**0.467**	0.002	0.104	0.001
Ti	**0.691**	0.009	0.000	0.005	0.000
V	0.127	0.000	0.014	0.157	**0.659**
Mn	**0.139**	0.104	0.070	0.092	0.006
Fe	**0.812**	0.008	0.000	0.001	0.001
Ni	0.101	0.041	0.024	**0.436**	0.239
Rb	**0.203**	0.008	0.185	0.106	0.002
Sr	0.171	**0.415**	0.167	0.001	0.000
Zr	0.017	0.006	**0.676**	0.000	0.002

Figure 1

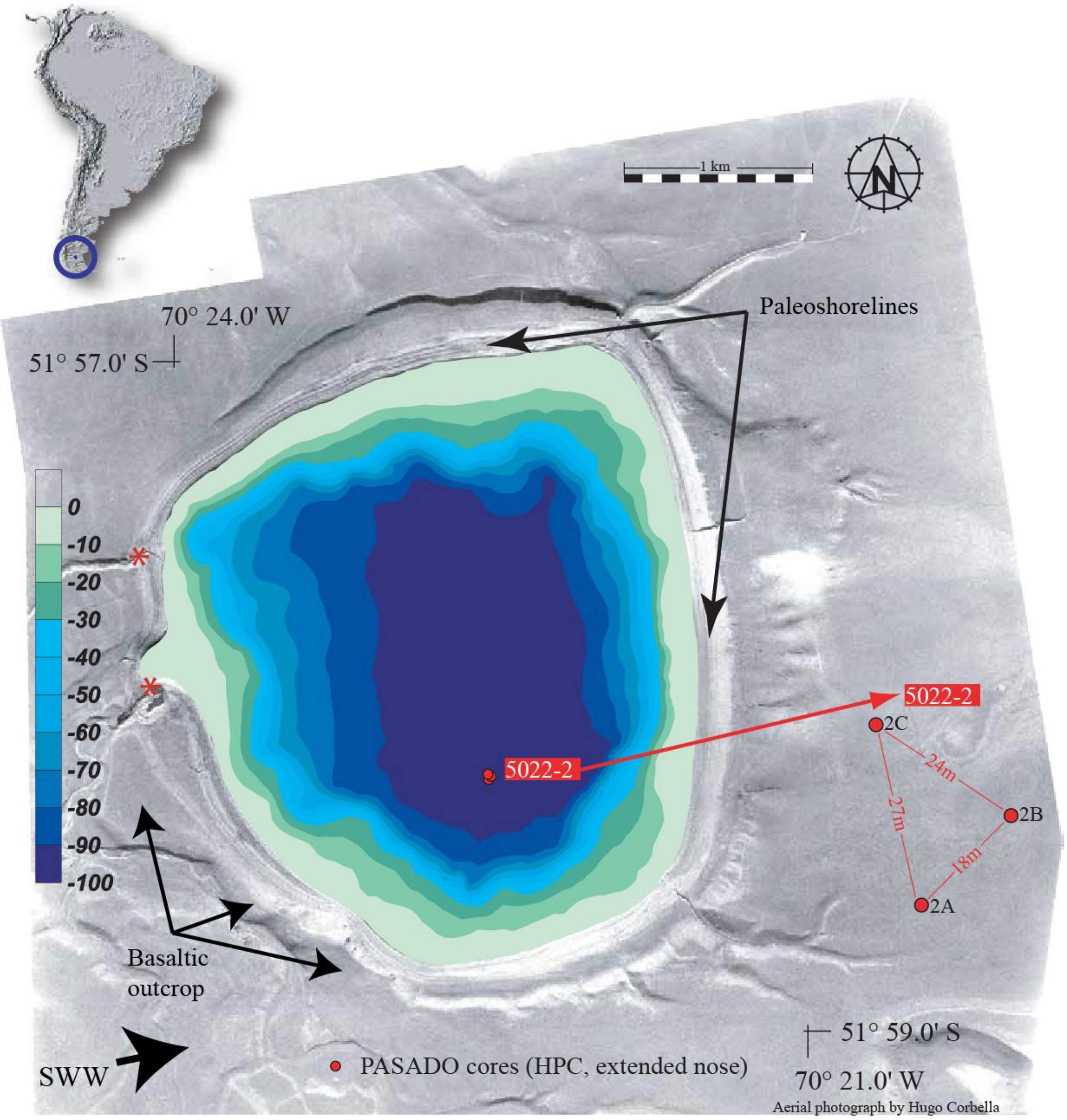

1 km
N
Paleoshorelines
70° 24.0' W
51° 57.0' S
0
-10
-20
-30
-40
-50
-60
-70
-80
-90
-100
5022-2
5022-2
2C
24m
27m
2B
18m
2A
Basaltic
outcrop
51° 59.0' S
70° 21.0' W
SWW
PASADO cores (HPC, extended nose)
Aerial photograph by Hugo Corbella

Figure 2

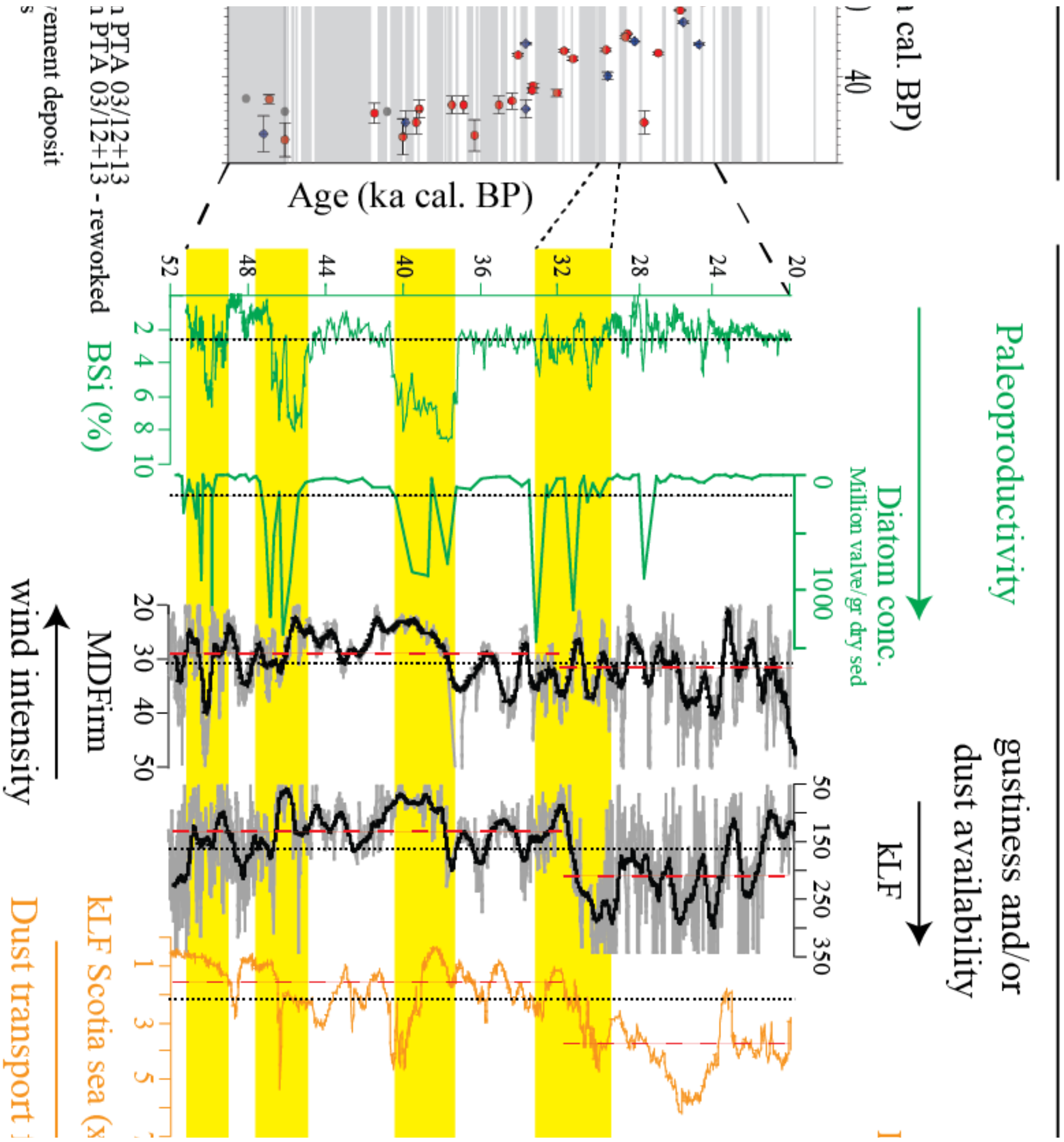
Paleoproductivity
gustiness and/or dust availability
Age (ka cal. BP)
BSi (%)
Diatom conc.
Million valve/gr dry sed
MDFirm
wind intensity
kLF
kLF Scotia sea
Dust transport

Figure 3

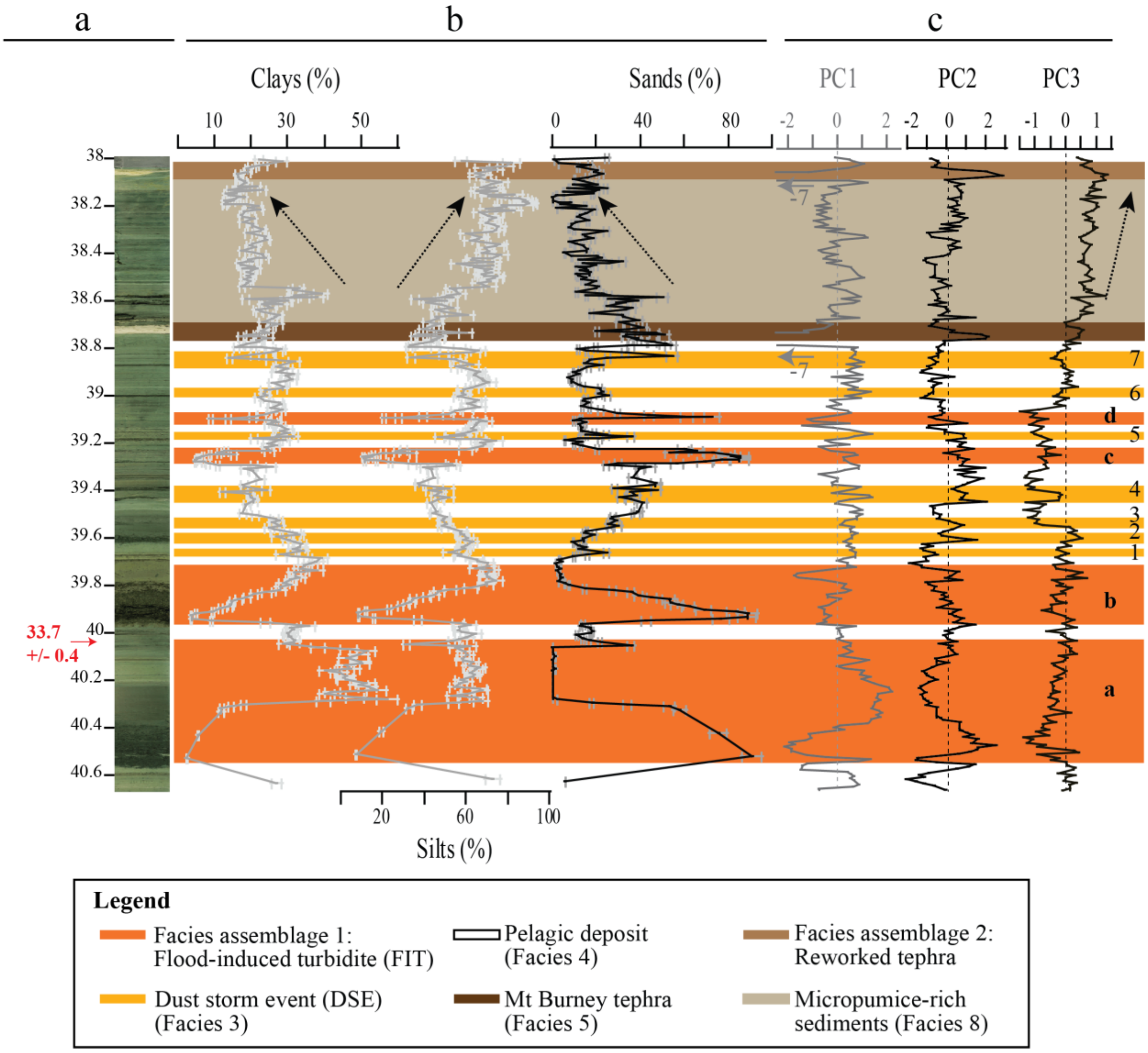
a
b
c
Clays (%)
Sands (%)
Silts (%)
PC1
PC2
PC3
33.7
+/- 0.4
Legend
Facies assemblage 1:
Flood-induced turbidite (FIT)
Pelagic deposit
(Facies 4)
Facies assemblage 2:
Reworked tephra
Dust storm event (DSE)
(Facies 3)
Mt Burney tephra
(Facies 5)
Micropumice-rich
sediments (Facies 8)

Figure 4

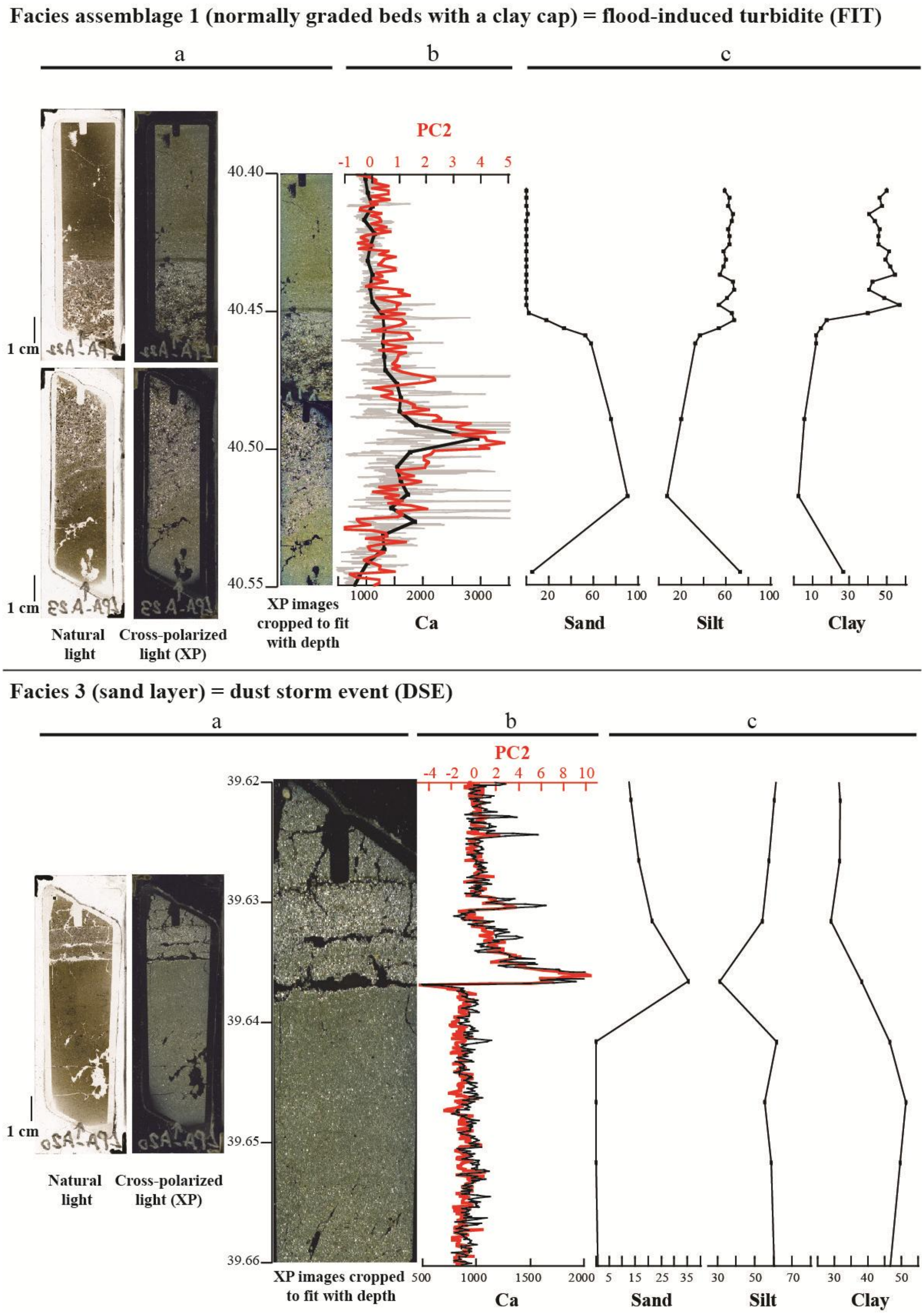
Facies assemblage 1 (normally graded beds with a clay cap) = flood-induced turbidite (FIT)
a
b
c
PC2
-1 0 1 2 3 4 5
40.40
40.45
40.50
40.55
1 cm
1 cm
Natural light
Cross-polarized light (XP)
XP images cropped to fit with depth
1000 2000 3000
Ca
20 60 100
Sand
20 60 100
Silt
10 30 50
Clay
Facies 3 (sand layer) = dust storm event (DSE)
a
b
c
PC2
-4 -2 0 2 4 6 8 10
39.62
39.63
39.64
39.65
39.66
1 cm
Natural light
Cross-polarized light (XP)
XP images cropped to fit with depth
500 1000 1500 2000
Ca
5 15 25 35
Sand
30 50 70
Silt
30 40 50
Clay

Facies 5 : Mt Burney tephra

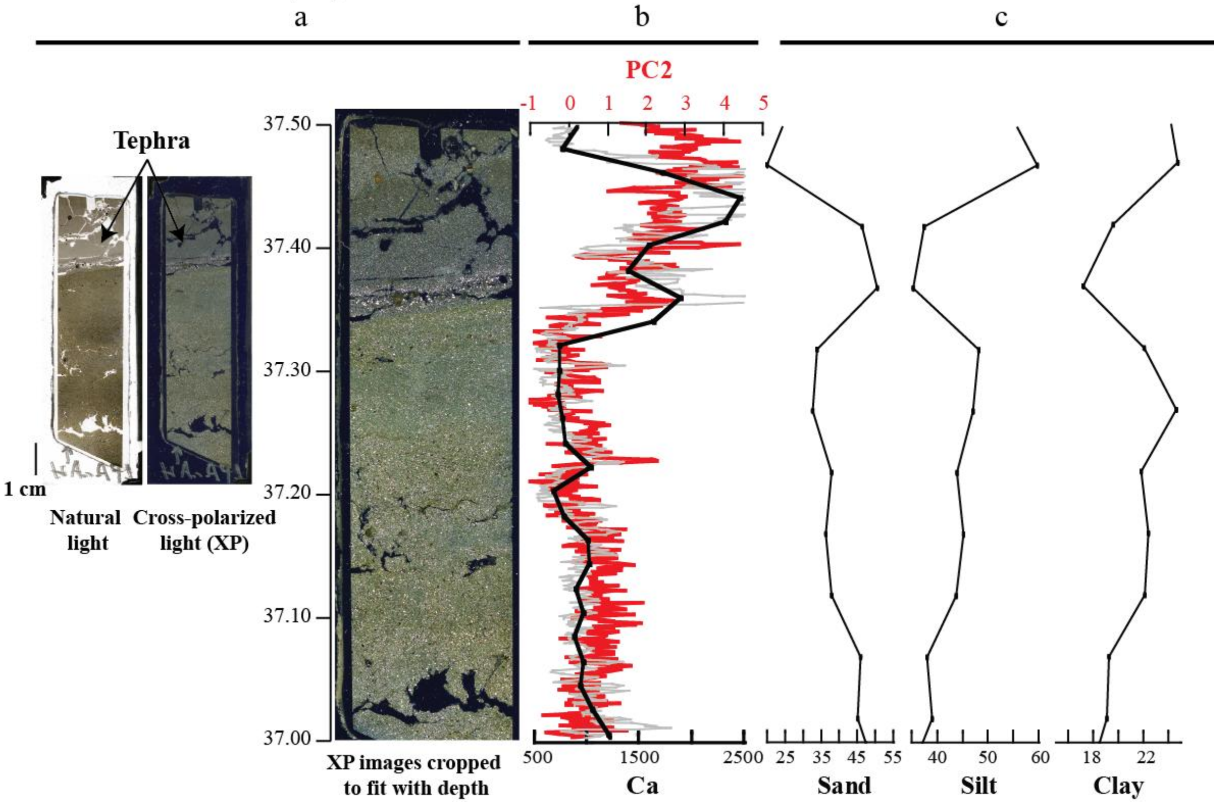

Figure 5

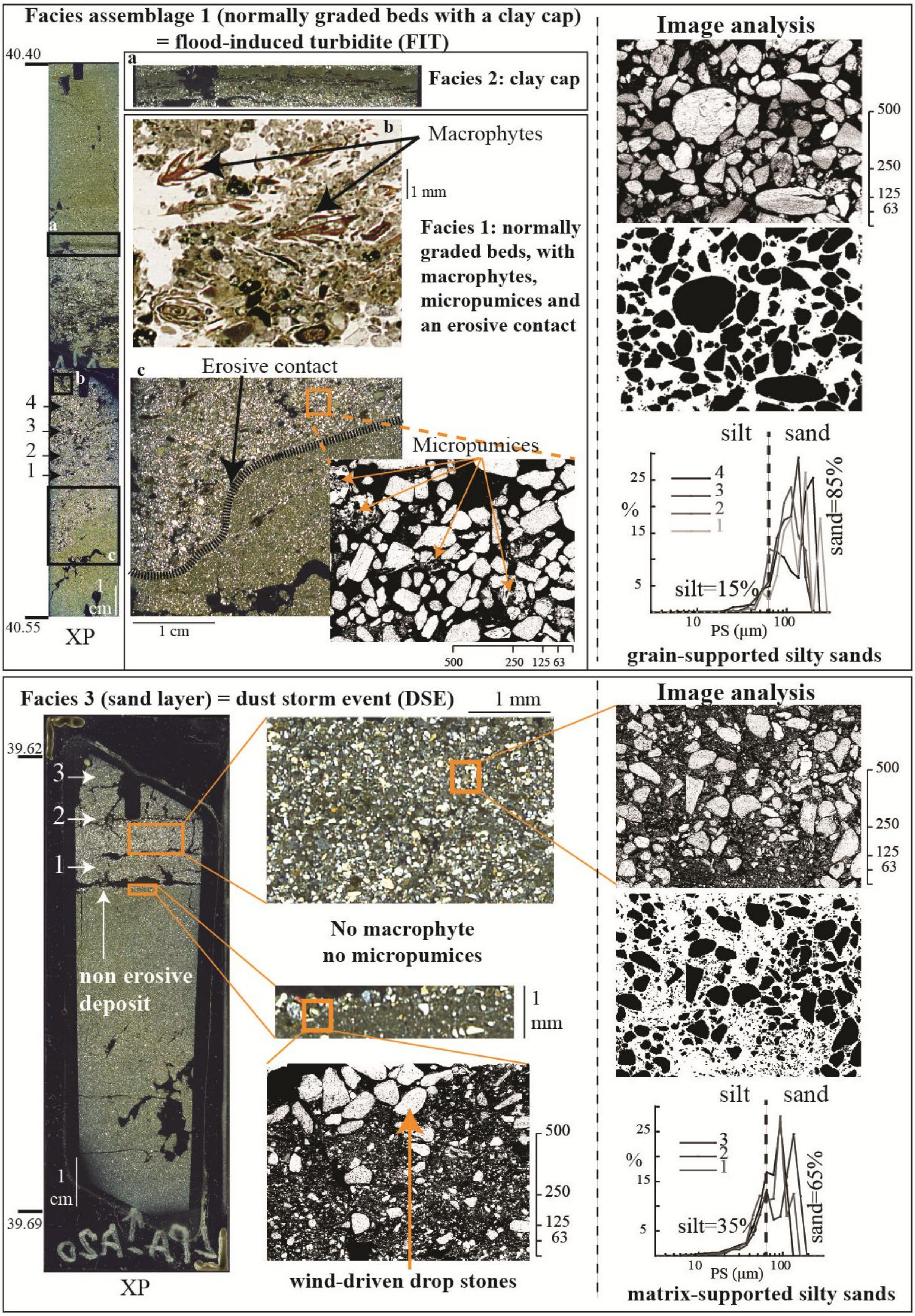

Facies assemblage 1 (normally graded beds with a clay cap)
= flood-induced turbidite (FIT)
40.40
a
Facies 2: clay cap
b
Macrophytes
1 mm
Facies 1: normally graded beds, with macrophytes, micropumices and an erosive contact
c
Erosive contact
Micropumices
4
3
2
1
1 cm
40.55
XP
1 cm
500
250
125
63
Image analysis
500
250
125
63
silt
sand
25
%
15
5
4
3
2
1
sand=85%
silt=15%
10
PS (µm)
100
grain-supported silty sands
Facies 3 (sand layer) = dust storm event (DSE)
1 mm
39.62
3
2
1
non erosive deposit
1 cm
39.69
XP
No macrophyte
no micropumices
1 mm
500
250
125
63
wind-driven drop stones
Image analysis
500
250
125
63
silt
sand
25
%
15
5
3
2
1
sand=65%
silt=35%
10
PS (µm)
100
matrix-supported silty sands

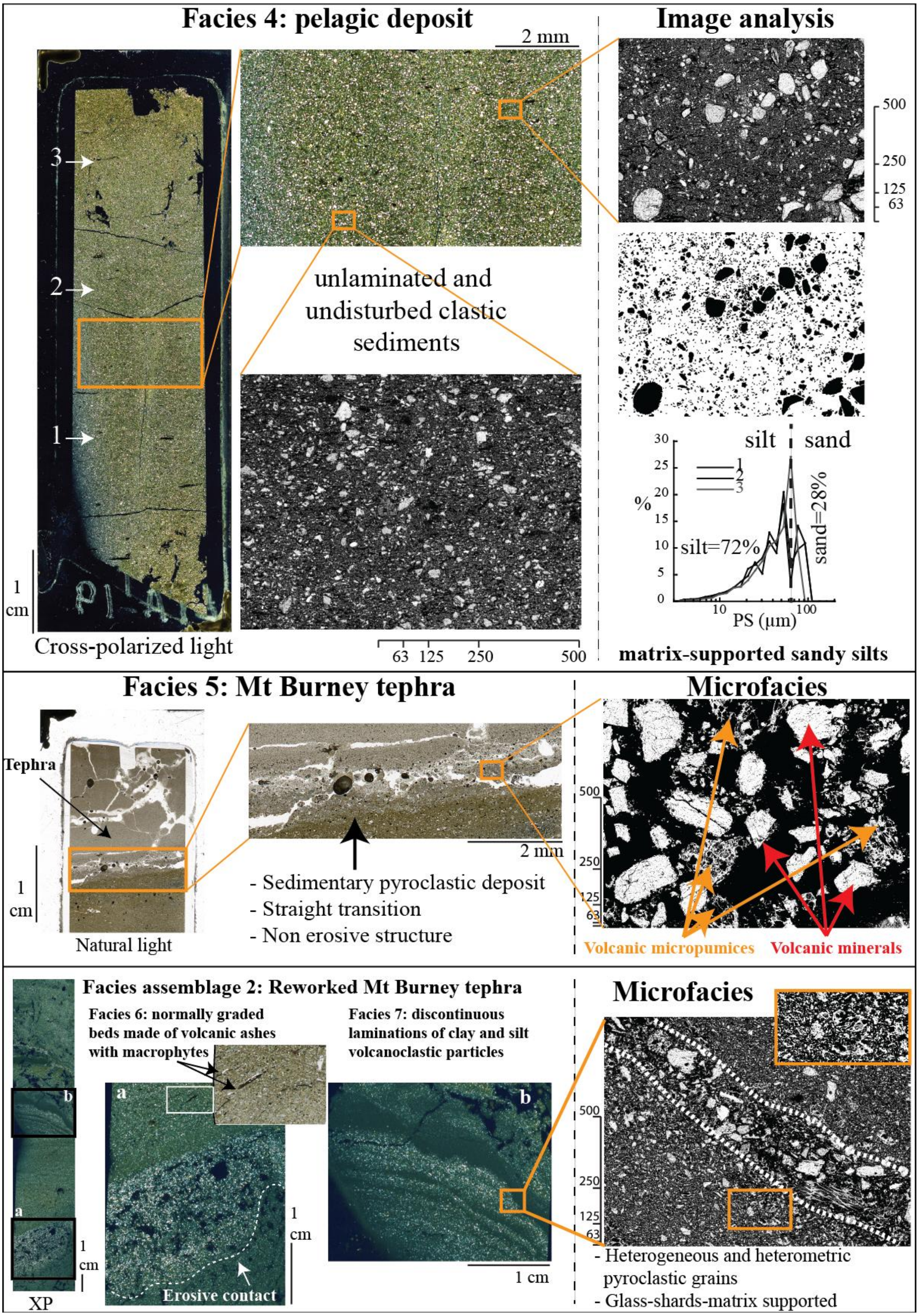

Facies 4: pelagic deposit
2 mm
3
2
1
1 cm
Cross-polarized light
unlaminated and undisturbed clastic sediments
63 125 250 500
Image analysis
500
250
125
63
30
25
20
15
10
5
0
%
silt
sand
1
2
3
silt=72%
sand=28%
10
100
PS (µm)
matrix-supported sandy silts
Facies 5: Mt Burney tephra
Tephra
1 cm
Natural light
2 mm
- Sedimentary pyroclastic deposit
- Straight transition
- Non erosive structure
Microfacies
500
250
125
63
Volcanic micropumices
Volcanic minerals
Facies assemblage 2: Reworked Mt Burney tephra
Facies 6: normally graded beds made of volcanic ashes with macrophytes
Facies 7: discontinuous laminations of clay and silt volcanoclastic particles
a
b
1 cm
XP
Erosive contact
1 cm
Microfacies
500
250
125
63
- Heterogeneous and heterometric pyroclastic grains
- Glass-shards-matrix supported

1035

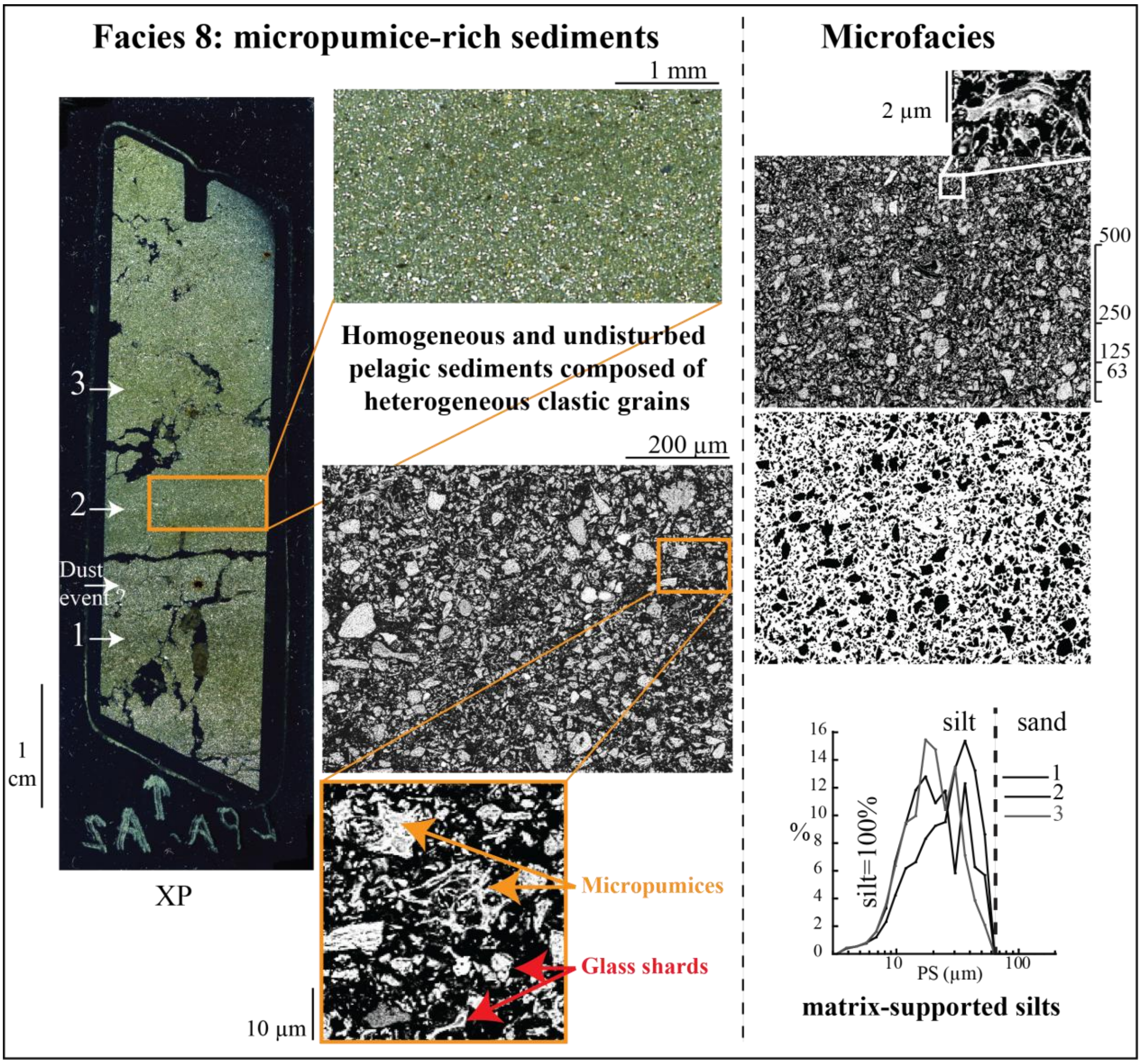

Facies 8: micropumice-rich sediments
Microfacies
1 mm
2 µm
500
250
125
63
3
2
Dust event ?
1
1 cm
Homogeneous and undisturbed pelagic sediments composed of heterogeneous clastic grains
200 µm
XP
Micropumices
Glass shards
10 µm
silt
sand
16
14
12
10
8
6
4
2
0
%
silt=100%
10
100
PS (µm)
1
2
3
matrix-supported silts

1036 Figure 6
1037

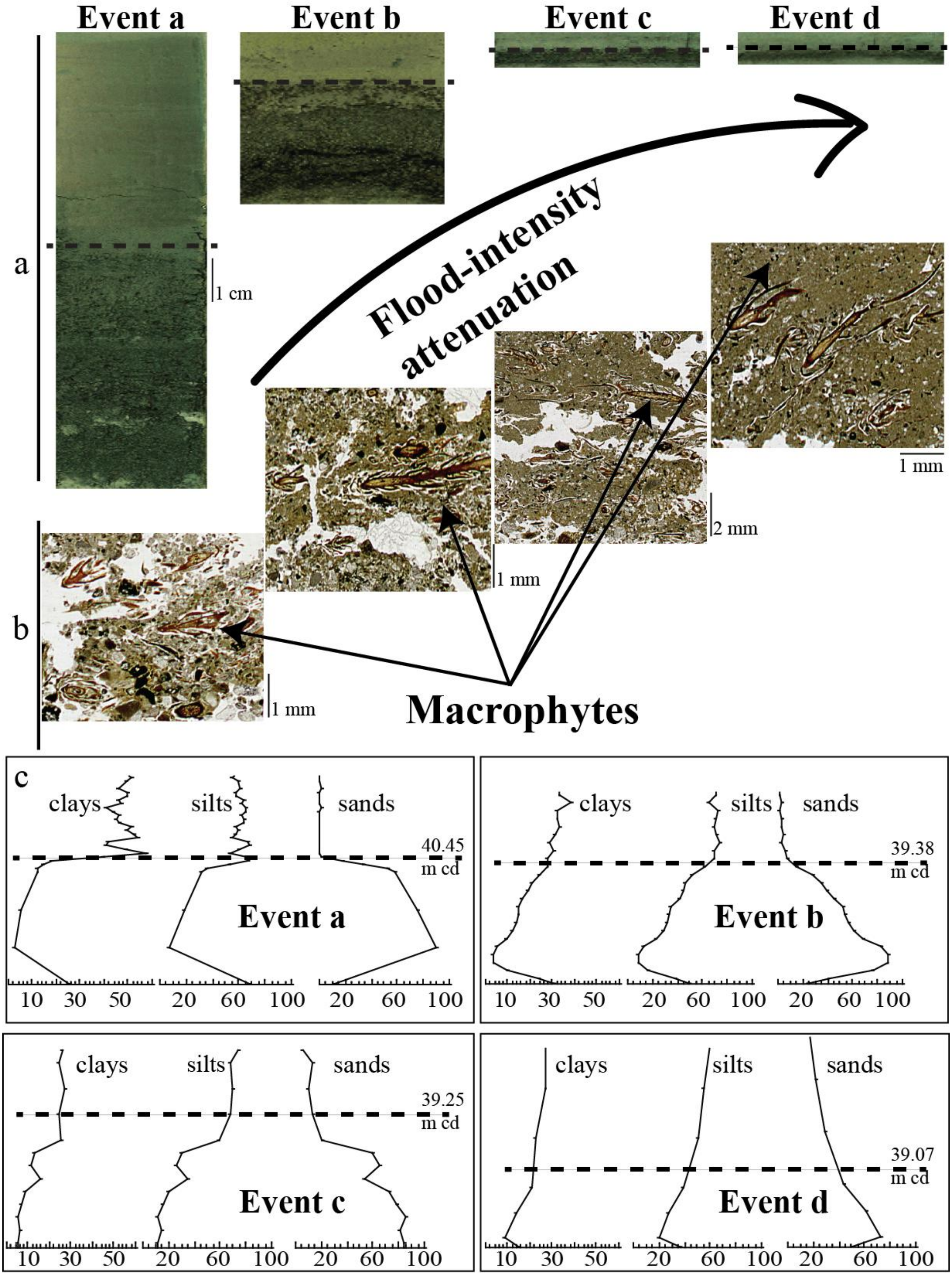

1038

Figure 7

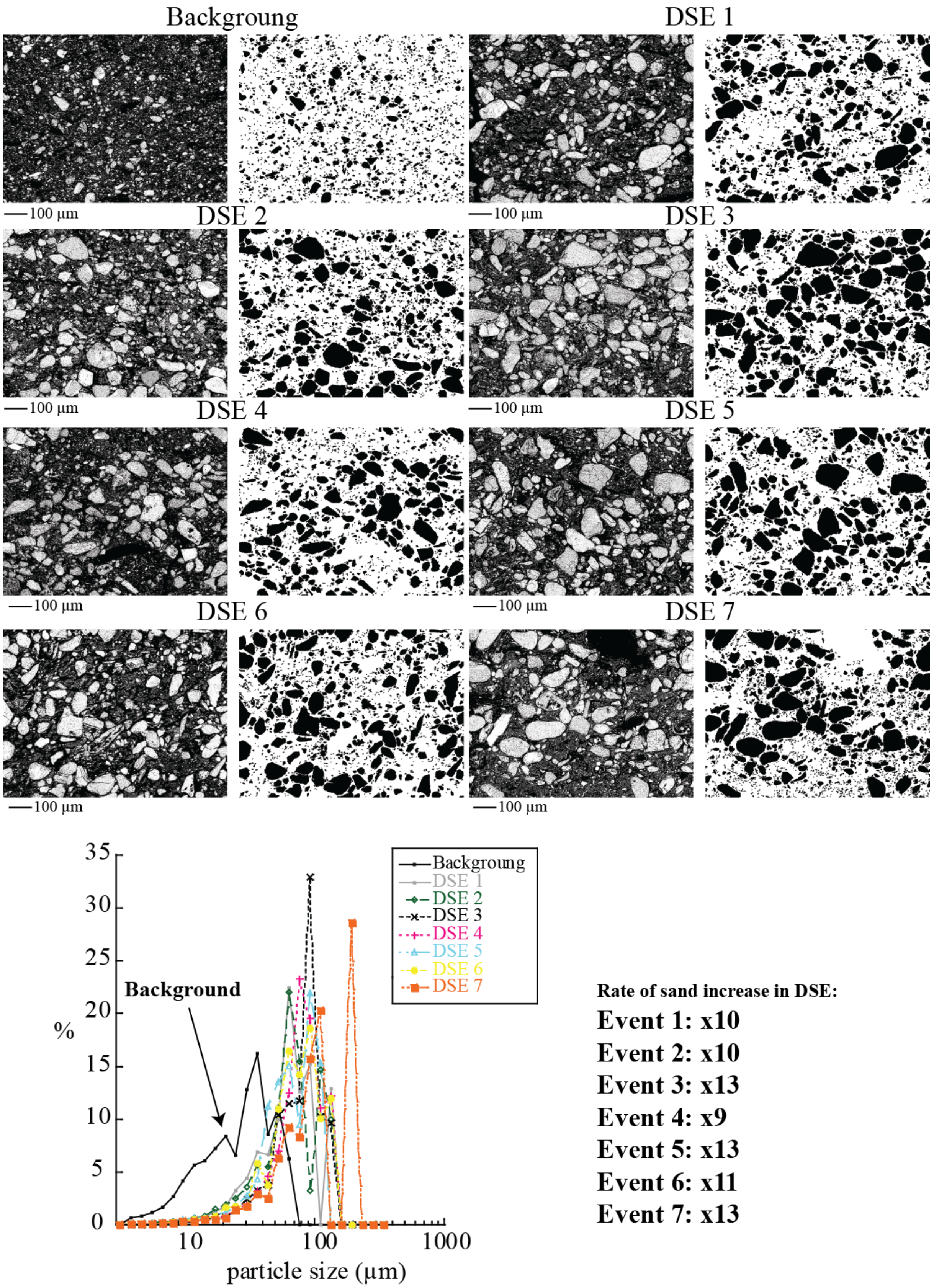
Backgroung
DSE 1
DSE 2
DSE 3
DSE 4
DSE 5
DSE 6
DSE 7
100 µm
%
particle size (µm)
Background
Backgroung
DSE 1
DSE 2
DSE 3
DSE 4
DSE 5
DSE 6
DSE 7
Rate of sand increase in DSE:
Event 1: x10
Event 2: x10
Event 3: x13
Event 4: x9
Event 5: x13
Event 6: x11
Event 7: x13

Figure 8


Macrophytes covering the shoreline
Canyon in the northwestern part of the lake
Fallen tephra layer
Gust of dust
West
East

Figure 9

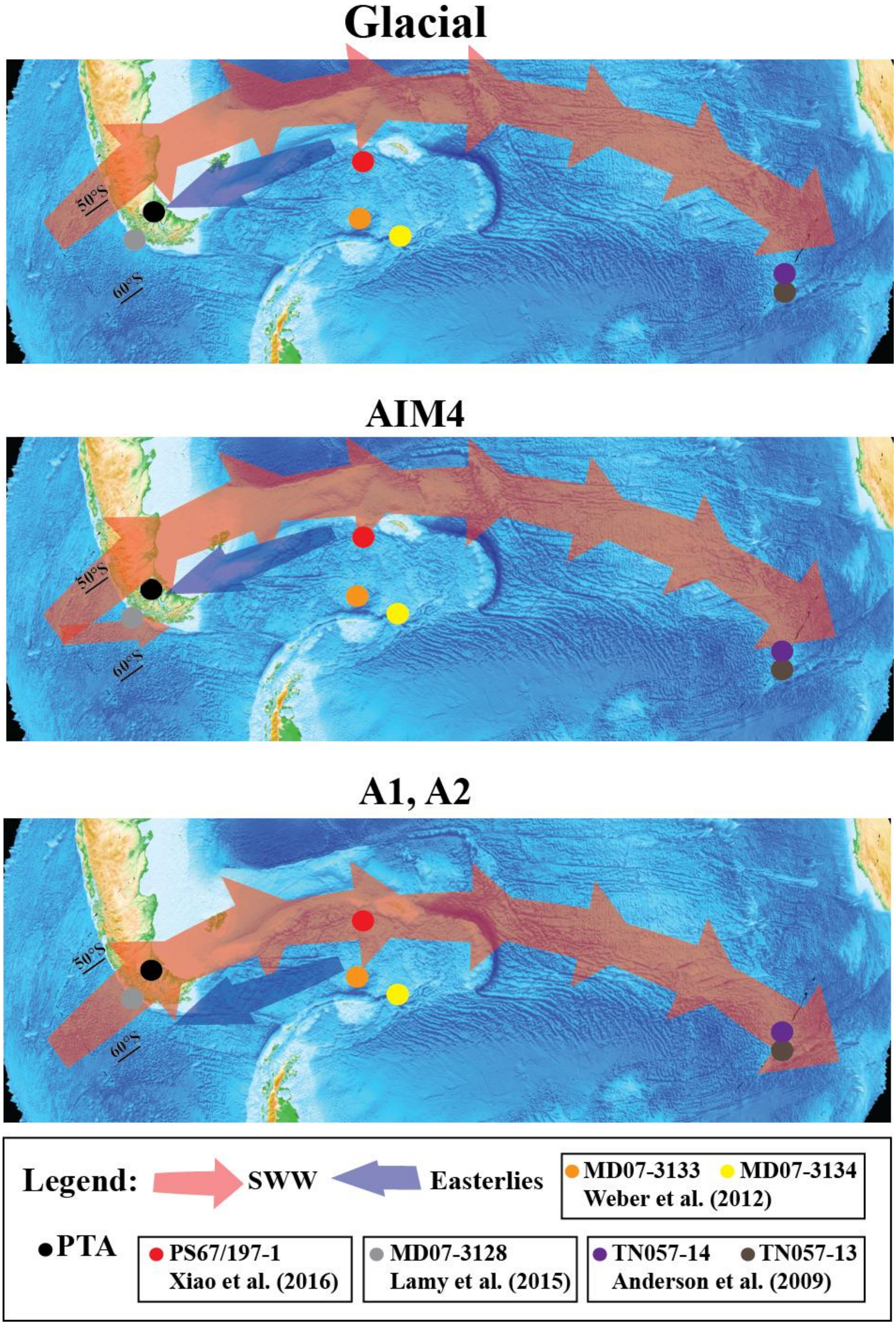
Glacial
50°S
60°S
AIM4
50°S
60°S
A1, A2
50°S
60°S
Legend:
SWW
Easterlies
MD07-3133
MD07-3134
Weber et al. (2012)
PTA
PS67/197-1
Xiao et al. (2016)
MD07-3128
Lamy et al. (2015)
TN057-14
TN057-13
Anderson et al. (2009)

Appendix A

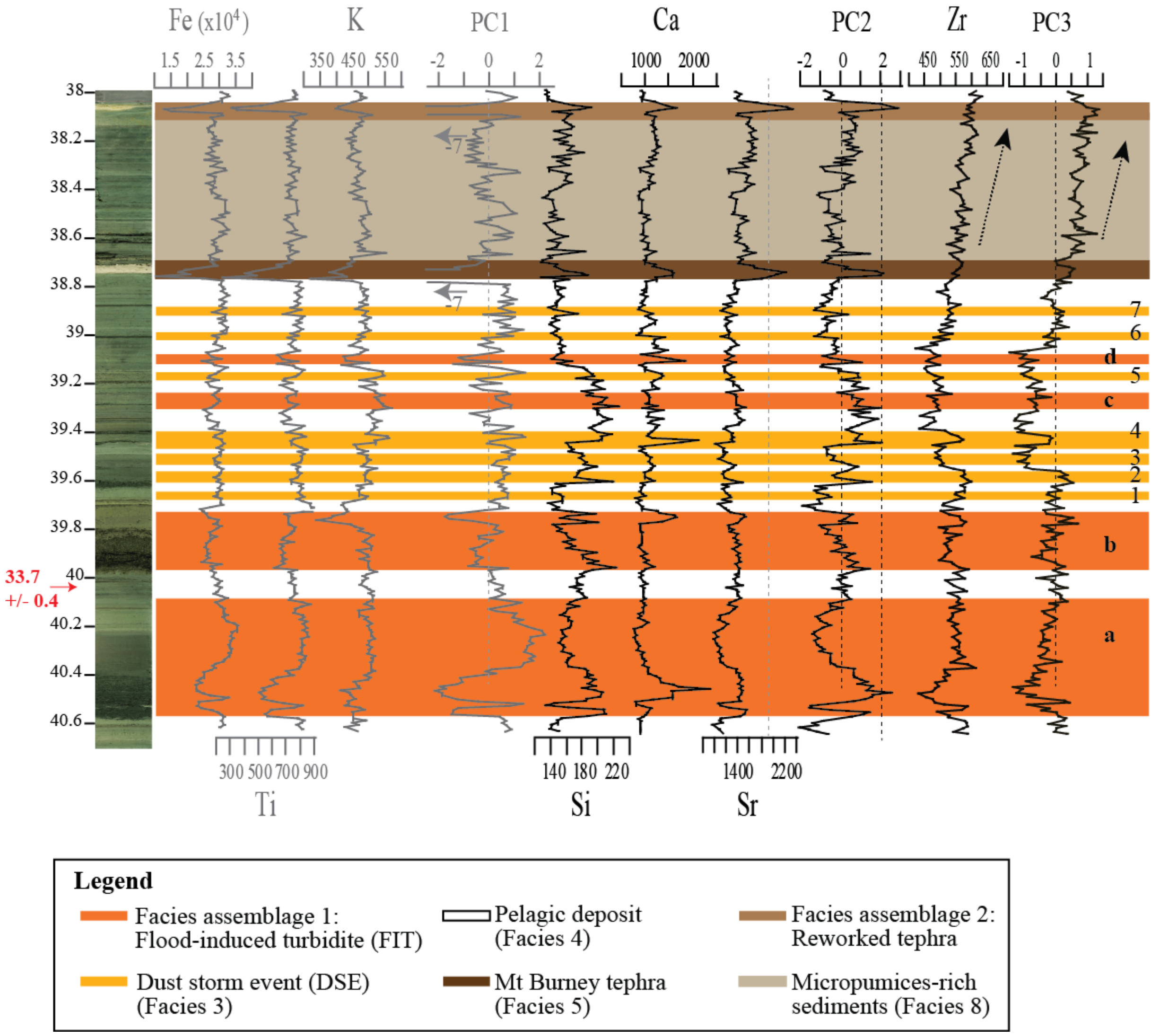

Fe (x10^4)
1.5 2.5 3.5
K
350 450 550
PC1
-2 0 2
Ca
1000 2000
PC2
-2 0 2
Zr
450 550 650
PC3
-1 0 1
38
38.2
38.4
38.6
38.8
39
39.2
39.4
39.6
39.8
40
40.2
40.4
40.6
33.7
+/- 0.4
-7
-7
7
6
d
5
c
4
3
2
1
b
a
300 500 700 900
Ti
140 180 220
Si
1400 2200
Sr
Legend
Facies assemblage 1: Flood-induced turbidite (FIT)
Pelagic deposit (Facies 4)
Facies assemblage 2: Reworked tephra
Dust storm event (DSE) (Facies 3)
Mt Burney tephra (Facies 5)
Micropumices-rich sediments (Facies 8)

Appendix B

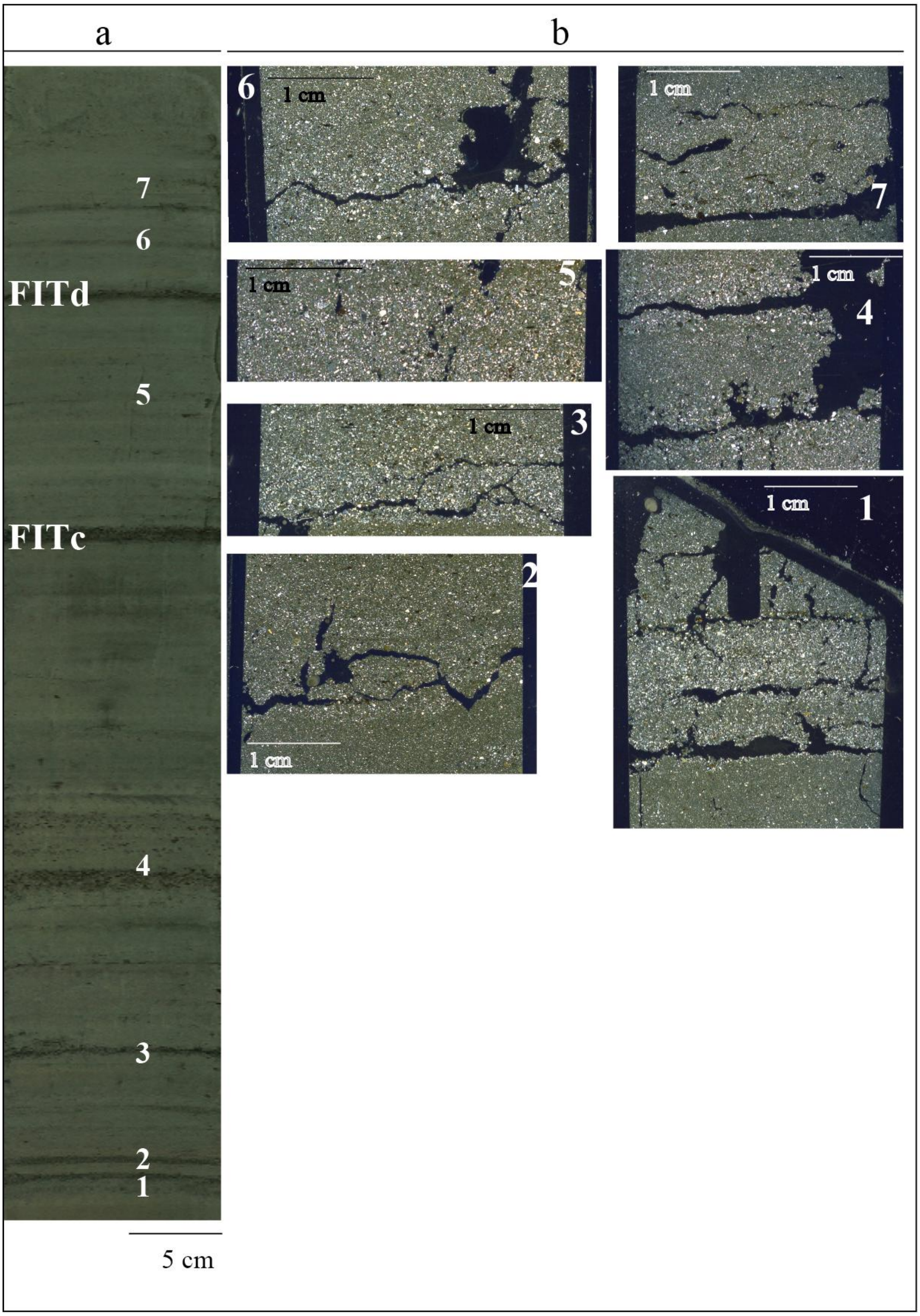

Appendix C

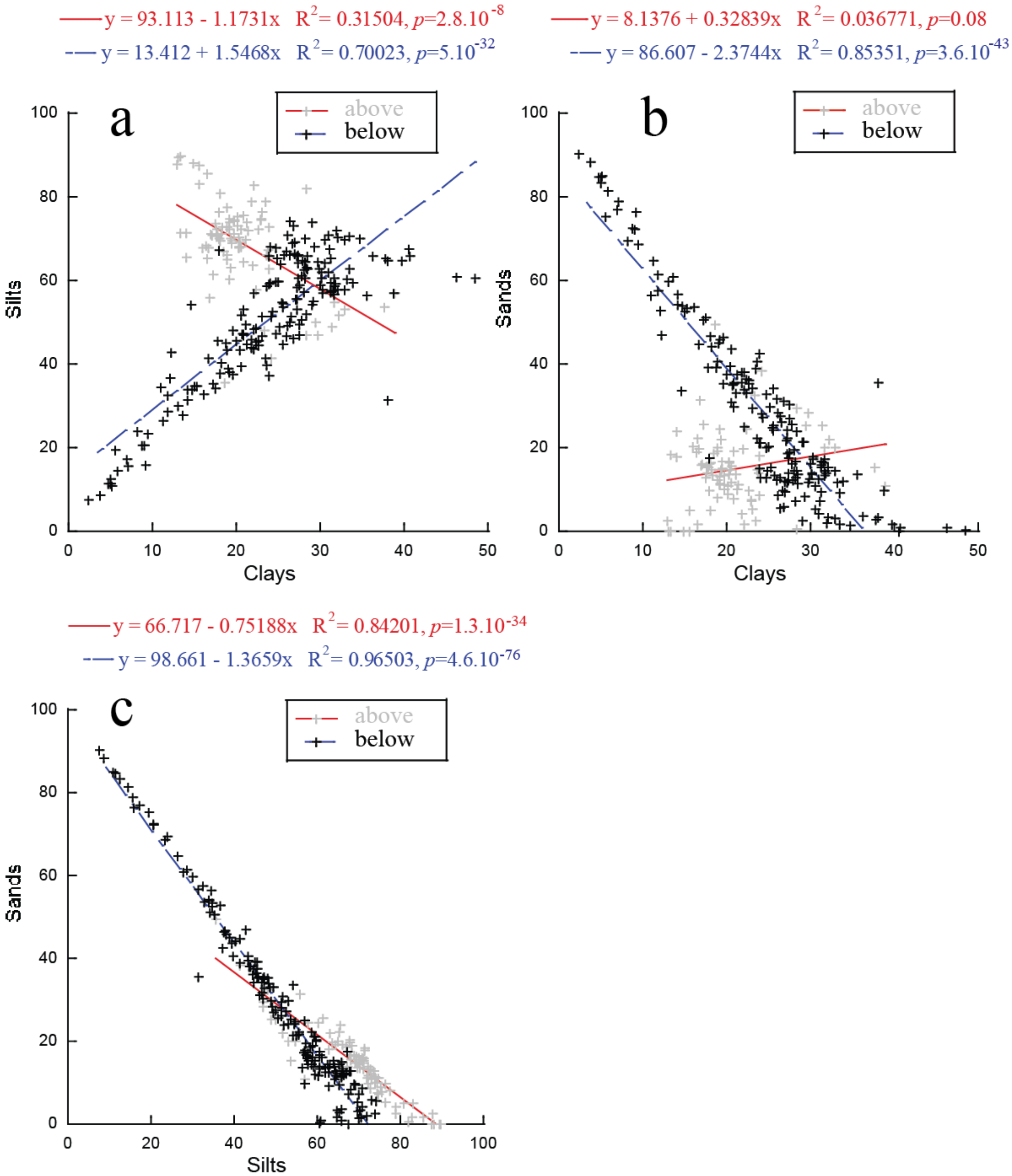

y = 93.113 - 1.1731x R2= 0.31504, p=2.8.10-8
y = 13.412 + 1.5468x R2= 0.70023, p=5.10-32
a
above
below
Silts
Clays
y = 8.1376 + 0.32839x R2= 0.036771, p=0.08
y = 86.607 - 2.3744x R2= 0.85351, p=3.6.10-43
b
above
below
Sands
Clays
y = 66.717 - 0.75188x R2= 0.84201, p=1.3.10-34
y = 98.661 - 1.3659x R2= 0.96503, p=4.6.10-76
c
above
below
Sands
Silts

Appendix D

a

Variable	Observations	Minimum	Maximum	Mean	standard deviation
Si	25960	11.000	479.000	165.741	35.178
K	25960	65.000	1171.000	479.670	62.582
Ca	25960	224.000	16933.000	1080.520	385.231
Ti	25960	56.000	2072.000	738.434	132.918
V	25960	0.000	181.000	48.017	21.607
Mn	25960	59.000	4614.000	473.747	148.861
Fe	25960	2324.000	65307.000	28815.947	4202.118
Ni	25960	0.000	378.000	67.178	33.682
Rb	25960	0.000	554.000	272.220	55.617
Sr	25960	210.000	2974.000	1361.389	243.005
Zr	25960	0.000	1925.000	543.068	99.733

Correlation matrix (Pearson (n)) :

Variables	Si	K	Ca	Ti	V	Mn	Fe	Ni	Rb	Sr	Zr
Si	1	0.429	0.276	0.062	0.018	0.216	0.013	-0.079	0.027	0.220	-0.083
K	0.429	1	0.084	0.455	0.121	0.221	0.548	0.064	0.259	-0.048	0.037
Ca	0.276	0.084	1	-0.113	-0.006	0.098	-0.105	-0.040	-0.048	0.381	0.004
Ti	0.062	0.455	-0.113	1	0.217	0.170	0.742	0.194	0.256	-0.337	0.107
V	0.018	0.121	-0.006	0.217	1	0.088	0.246	0.078	0.104	-0.081	0.053
Mn	0.216	0.221	0.098	0.170	0.088	1	0.283	0.063	0.073	-0.025	-0.026
Fe	0.013	0.548	-0.105	0.742	0.246	0.283	1	0.232	0.324	-0.392	0.129
Ni	-0.079	0.064	-0.040	0.194	0.078	0.063	0.232	1	0.082	-0.148	0.063
Rb	0.027	0.259	-0.048	0.256	0.104	0.073	0.324	0.082	1	0.011	0.159
Sr	0.220	-0.048	0.381	-0.337	-0.081	-0.025	-0.392	-0.148	0.011	1	0.210
Zr	-0.083	0.037	0.004	0.107	0.053	-0.026	0.129	0.063	0.159	0.210	1

b

	PC1	**PC2**	**PC3**								
	F1	F2	F3	F4	F5	F6	F7	F8	F9	F10	F11
Si	0,099	0,555	-0,272	-0,107	-0,023	-0,192	-0,052	-0,478	-0,440	0,314	0,193
K	0,411	0,319	-0,109	-0,239	-0,071	-0,211	-0,130	-0,141	0,304	-0,619	-0,314
Ca	-0,082	0,511	0,038	0,327	-0,029	-0,190	-0,052	0,710	-0,257	-0,104	-0,059
Ti	0,499	-0,070	0,004	-0,072	-0,008	-0,082	-0,248	0,212	0,145	0,647	-0,434
V	0,214	-0,007	0,104	0,403	0,849	-0,129	0,108	-0,165	-0,002	-0,056	-0,036
Mn	0,224	0,241	-0,237	0,308	-0,084	0,827	0,171	-0,049	0,032	-0,019	-0,129
Fe	0,541	-0,066	0,012	-0,024	-0,030	0,041	-0,137	0,219	0,112	-0,043	0,787
Ni	0,191	-0,152	0,139	0,671	-0,511	-0,325	0,165	-0,274	0,030	-0,009	-0,027
Rb	0,270	0,067	0,385	-0,331	-0,043	-0,020	0,781	0,094	-0,198	0,032	-0,057
Sr	-0,248	0,481	0,367	0,032	0,005	0,007	0,064	-0,104	0,678	0,263	0,164
Zr	0,078	0,060	0,737	-0,018	-0,048	0,260	-0,464	-0,176	-0,336	-0,118	-0,066